LANGMUIR

pubs.acs.org/Langmuir Article

Protein Corona Formation and Aggregation of Amyloid β 1−40-Coated Gold Nanocolloids

Kazushige Yokoyama,* Eli Barbour,† Rachel Hirschkind,† Bryan Martinez Hernandez,† Kaylee Hausrath,† and Theresa Lam†

Cite This: *Langmuir* 2024, 40, 1728−1746 Read Online

ACCESS | Metrics & More | Article Recommendations | Supporting Information

ABSTRACT: Amyloid fibrillogenesis is a pathogenic protein aggregation process that occurs through a highly ordered process of protein−protein interactions. To better understand the protein−protein interactions involved in amyloid fibril formation, we formed nanogold colloid aggregates by stepwise additions of ∼2 nmol of amyloid β 1−40 peptide ($A\beta_{1-40}$) at pH ∼3.7 and ∼25 °C. The processes of protein corona formation and building of gold colloid [diameters (d) of 20 and 80 nm] aggregates were confirmed by a red-shift of the surface plasmon resonance (SPR) band, λ_{peak}, as the number of $A\beta_{1-40}$ peptides [$N(A\beta_{1-40})$] increased. The normalized red-shift of λ_{peak}, $\Delta\lambda$, was correlated with the degree of protein aggregation, and this process was approximated as the adsorption isotherm explained by the Langmuir−Freundlich model. As the coverage fraction (θ) was analyzed as a function of ϕ, which is the $N(A\beta_{1-40})$ per total surface area of nanogold colloids available for adsorption, the parameters for explaining the Langmuir−Freundlich model were in good agreement for both 20 and 80 nm gold, indicating that ϕ could define the stage of the aggregation process. Surface-enhanced Raman scattering (SERS) imaging was conducted at designated values of ϕ and suggested that a protein−gold surface interaction during the initial adsorption stage may be dependent on the nanosize. The 20 nm gold case seems to prefer a relatively smaller contacting section, such as a −C−N or C═C bond, but a plane of the benzene ring may play a significant role for 80 nm gold. Regardless of the size of the particles, the β-sheet and random coil conformations were considered to be used to form gold colloid aggregates. The methodology developed in this study allows for new insights into protein−protein interactions at distinct stages of aggregation.

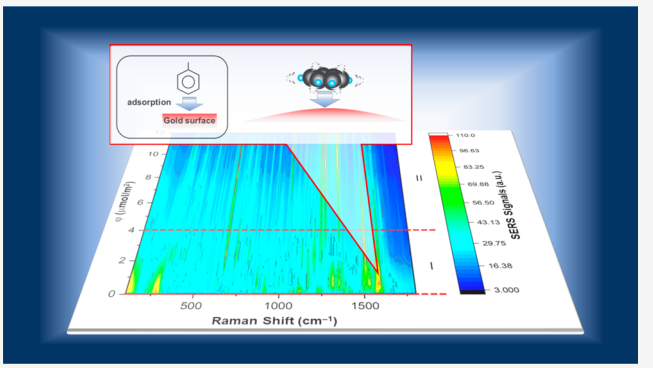

INTRODUCTION

One way in which Alzheimer's disease (AD) is thought to develop is based on the amyloid cascade hypothesis, in which fibrils composed of several hundred amyloid plaques form, which reach a size of micrometers[1−6] and disrupt the function of brain cells. The main components of amyloid aggregates found in the brains of AD patients are amyloid β peptides (Aβs).[7,8] There are several forms of Aβs that differ in the number of amino acid residues. The progression of AD is associated with the formation of amyloid β 1−40 ($A\beta_{1-40}$) or amyloid β 1−42 ($A\beta_{1-42}$).[9−21] The $A\beta_{1-40}$ or $A\beta_{1-42}$ peptides have an amphipathic sequence comprising a polar N-terminal region (residues 1−16), followed by a central hydrophobic core (residues 17−21), a polar region (residues 22−29), and a nonpolar C-terminal region (residues 30−40 or −42, respectively). Of $A\beta_{1-40}$ and $A\beta_{1-42}$, $A\beta_{1-40}$ is produced at higher levels,[22] but $A\beta_{1-42}$ is more toxic.[23−28] The onset of the aggregation event involves a soluble intermediate phase of disordered oligomers,[6,14,29,30] which then convert into highly ordered and insoluble fibrils.[31−41] This transition to the intermediate phase was not been well-characterized. The oligomer is considered to require ∼40 kJ/mol of activation energy[42,43] before fibril formation occurs, but once oligomers have been formed, they proceed nonreversibly to form prefibrils. Technical limitations have impaired the development of experimental conditions for interrogating the stabilization of the initial oligomers, which has limited the insights into this process. However, the Aβ fibrils have been studied extensively because they are insoluble,[34,44−46] which makes it easier to work with them thanwith their soluble monomeric and oligomeric counterparts.[47,48] Several strategies have been employed to characterize the structure of the monomer, but these involve the use of physicochemical conditions that are unfavorable for aggregation.

Received: September 28, 2023
Revised: December 11, 2023
Accepted: December 12, 2023
Published: January 9, 2024

https://doi.org/10.1021/acs.langmuir.3c02923
Langmuir 2024, 40, 1728−1746

Extensive studies using molecular dynamics (MD) simulation have characterized the aggregation and disaggregation of Aβ[49−70] and provided insights into the oligomerization process.[66,71−87] Secondary structures found to be formed by Aβ_{1-40} dimers include intra- and intermolecular β-sheet and α-helix structures.[83] The Aβ peptide exists predominantly as a random coil under physiological conditions.[88−91] The mechanism and dynamics of aggregation are affected by the concentration of the interacting species and the accessibility of sites for interaction. The resulting interactions can be either electrostatic or hydrophobic, and fibrils grow through their interaction with a monomer.[71]

The aggregation process has been extensively examined by various approaches to predict the protein polymerization process.[92−99] Typically, the progression of protein aggregation follows a sigmoidal curve that can be fitted by many mathematical functions.[95,100] This system has been analyzed by the Ferrone model (postulating the presence of secondary events),[101,102] the Finke−Watzky model (nucleation followed by autocatalytic surface growth),[103] and the Knowles analytical equation of the mechanistic model (combination of primary nucleation, secondary nucleation, fibril elongation, and fibril fragmentation).[104] A common mechanistic model is nucleation-dependent polymerization (a simple two-step mechanism), in which the nucleation from soluble proteins is slower than the elongation step, although this has not been demonstrated experimentally. In contrast, models of secondary nucleation processes in fibril fragmentation are well-accepted[41,98,104,105] and have been proposed for Aβ.[10,13,22,106,107] The aggregation kinetics of the Aβ_{1-40} peptide were characterized using a synergistic approach of nuclear magnetic resonance (NMR), thioflavin T fluorescence, transmission electron microscopy (TEM), and dynamic light scattering. The current consensus with respect to the aggregation process is that oligomers with relatively high molecular weights are slowly formed, followed by conversion into more compact fibril nuclei. Then, fast formation of additional fibrils nuclei occurs through fibril surface-catalyzed processes. Finally, fibrils grow by addition of soluble Aβ species to form large aggregates.[108]

Our approach aims to focus on detecting protein−protein interactions and characterizing oligomer formation. To do so, we prepared a protein corona of Aβ_{1-40} over a nanogold colloid, which allows Aβ_{1-40} peptides to interact with each other over the gold surface but inhibits the fibril formation of Aβ_{1-40} and instead forms gold colloid aggregates.[109−116] The formation of gold colloid aggregates is strongly indicative of a protein adsorption process over the nanoparticles to form a protein corona. Considerable attention has been paid to protein corona formation due to its potential use in designing new bionanomaterials[117−119] and its immunologic properties.[120−123] A layer of protein corona can typically be divided into either hard or soft coronas of the proteins, depending on whether the binding affinity to the nanoparticle is relatively strong or weak, respectively.[124] The adsorption to the gold nanoparticle removes one degree of freedom for networking, resulting in a barrier to further polymerization. The adsorption of the hydrophobic end (i.e., C-terminus) on the nanogold surface stabilizes the peptide by ∼10 kJ/mol.[125]

The Aβ_{1-40} peptide is known to form well-defined unfolded or folded conformations under acidic or basic conditions.[126,127] For example, when the Aβ_{1-40} monomer holds the folded conformation in basic or neutral pH ranges, Aβ_{1-40}-coated gold nanoparticles remain as individual dispersed particles. In contrast, acidic pH conditions induce an unfolded conformation of Aβ_{1-40}, which results in peptide networking between the Aβ_{1-40} peptides over gold nanoparticle surfaces, which causes the formation of gold colloid aggregates. The dispersed gold colloid exhibits a clear surface plasmon resonance (SPR) band peak at ∼530 nm, and the aggregated gold nanoparticles show a drastic red-shift in the SPR band to ∼630 nm. Therefore, the Aβ_{1-40} peptide-folded and -unfolded conformations can be investigated using coated gold nanoparticles and measuring the SPR band shift.[128−133] Remarkably, Aβ_{1-40} monomer-coated gold colloid particles exhibit a reversible self-assembly process in response to an external change in pH. This indicates that the formation of oligomers is a reversible process and an equilibrium exists between Aβ monomers and oligomers. This pH-induced reversible self-assembly is strongly dependent on the size of the gold colloid, and specifically, only 20 nm diameter gold colloids exhibit reversible self-assembly.[128−133]

Many experimental approaches have been taken to interrogate the aggregation process.[134−138] However, the self-assembly mechanism at the molecular level has not yet been elucidated.[95] A better understanding of the aggregation process is necessary to characterize the protein−protein interactions at each aggregation stage to better understand the molecular mechanism of the cause and progression of AD. In this work, we combined spectroscopic and microscopic approaches to examine the nucleation stage of the gold colloid aggregates and surface-enhanced Raman scattering (SERS) imaging to examine protein−protein interactions involved in each aggregation process. The average peak position of the SPR band, λ_{peak}, can be used as an indication of whether gold colloid aggregates are formed. We used an approach of monitoring the λ_{peak} as a function of the number of Aβ_{1-40} molecules [N(Aβ_{1-40})] at a constant pH and determined whether Aβ_{1-40}-coated gold colloid aggregates were formed. We increased N(Aβ_{1-40}) through stepwise addition to control the stage of the aggregation of Aβ_{1-40}-coated gold colloids and to extract the modes responsible for a particular interaction at different stages of gold colloid aggregations.

EXPERIMENTAL SECTION

Gold colloids and Aβ_{1-40} were prepared as described previously.[139] Briefly, at 25 ± 0.3 °C, the gold colloid of a particular diameter, d, was prepared at pH 3.7 ± 1.0 by addition of predetermined volumes of hydrochloric acid (HCl). The stock solution of Aβ_{1-40} was added in increments of 2 pmol initially, increasing to 200 pmol close to the end of the process, until a total of ∼1.5 nmol was reached. The absorption spectrum around the SPR band of the gold colloid was measured as a function of increasing N(Aβ_{1-40}). Each spectrum was collected over ∼4 min after N(Aβ_{1-40}) was increased.

For Raman imaging measurements, 500 μL each of 20 and 80 nm gold at pH 3.7 ± 0.3 with an N(Aβ_{1-40}) value of 0, 1.7, 8.4, 33.5, 167, or 700 pmol were deposited over a mica disc (10 mm diameter) followed by vaporization of the water overnight. Raman spectra were collected by using a WITec Raman alpha300R (WITec Oxford Instruments) confocal Raman imaging system. The microscope was set to automatic scanning of the specimen using a computer-controlled sample stage. A laser with a wavelength of 633 nm at a power of 0.60 ± 0.05 mW was used for excitation through a 100× objective lens (Zeiss, 0.9 numerical aperture). Raman-scattered photons were collected through a photonic fiber and directed to a 300 mm spectrograph equipped with a 600 grating/mm and a thermoelectrically cooled charge-coupled device detector. To conduct the experiments, a grid consisting of 100 pixels × 100 pixels covering an area of 20 μm × 20 μm was selected over the white-light image, and 10 000 spectra/map with an integration time of 500 ms/spectrum and a lateral spatial resolution of 0.43 μm were

https://doi.org/10.1021/acs.langmuir.3c02923
Langmuir 2024, 40, 1728−1746

acquired. The Raman spectrum in the range of 250−2900 cm^{-1} was collected

RESULTS AND DISCUSSION

The ultraviolet−visible (UV−vis) absorption spectra as a function of an increasing $N(A\beta_{1-40})$ are shown in Figure 1 for 20 nm gold (a) and 80 nm gold (b). For both conditions, the SPR band exhibited a red-shift as $N(A\beta_{1-40})$ increased. All spectra were processed with a component of the band expressed by a Gaussian profile by the Peak Fit function of OriginPro 2018b (Origin Lab), and the spectrum area-weighted average peak position, λ_{peak}, in the region between 450 and 850 nm was extracted,[139] as shown in Figure 2i for the 20 nm gold colloid with red dots and the 80 nm gold colloid with blue dots. The asymptotic feature of λ_{peak} toward the terminal region, λ_{max}, of $N(A\beta_{1-40})$ strongly indicated the completion of the aggregation, where the maximum amount of $A\beta_{1-40}$ was considered to be adsorbed over the gold colloid surface. The data indicate that aggregation occurred and λ_{max} was reached at a lower $N(A\beta_{1-40})$ for 80 nm gold than for 20 nm gold. However, the data plotted in Figure 2i describe the degree of aggregation as a function of the amount of $A\beta_{1-40}$ present, but they do not correctly reflect the quantitative progression of the aggregation because the available surface area for the $A\beta_{1-40}$ adsorption between 20 and 80 nm gold is different.

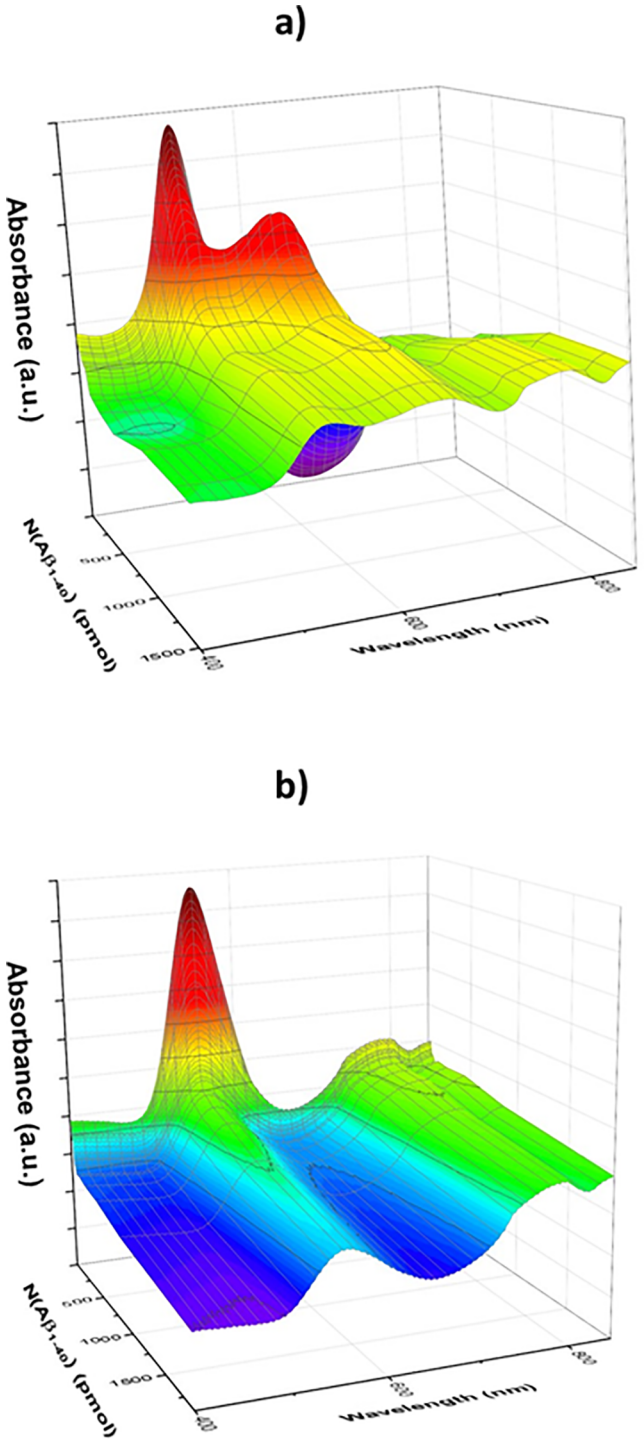

Figure 1. Absorption band as a function of externally added $A\beta_{1-40}$, $N(A\beta_{1-40})$, for (a) 20 nm gold and (b) 80 nm gold colloids.

To account for the adsorption surface area, we conducted the analysis on the basis of the amount of $A\beta_{1-40}$ for a unit area, $\phi = N(A\beta_{1-40})/A_{total}$, where A_{total} is the total available surface area (square meters) of gold colloids for adsorption. Adopting the Langmuir isotherm model,[140] we hypothesized that the difference between λ_{peak} and λ_{max} corresponded to the fraction of coverage, θ, as

$$\theta = \frac{\Delta\lambda(\phi)}{\Delta\lambda_{max}} = \frac{\lambda_{max} - \lambda_{peak}(\phi)}{\lambda_{max} - \lambda_{min}} = \frac{\theta(\phi)}{\theta_{max}} \quad (1)$$

where θ_{max} is the maximum adsorption or coverage of the $A\beta_{1-40}$ over the gold surface and $\theta(\phi)$ is the fraction of the coverage at a given ϕ. A_{total} is $N_{Au}A_{Au}(d)$, where N_{Au} is a total number of gold colloids and $A_{Au}(d)$ is a surface area of each gold colloid with diameter d assuming a spherical shape. The values of N_{Au} were adopted from previously reported work;[141] $N_{Au} = 1.4 \times 10^{11}$ particles/mL for 20 nm gold colloids, and $N_{Au} = 2.2 \times 10^{9}$ particles for 80 nm gold colloids. $N(A\beta_{1-40})$ and ϕ are related as follows: (a) $N(A\beta_{1-40}) = 0.0$ pmol and ϕ(Au 20 nm, $(\mathbf{1})_{20}$) = ϕ(Au 80 nm, $(\mathbf{1})_{80}$) = 0.0 μmol/m^2, (b) $N(A\beta_{1-40}) = 1.7$ pmol, ϕ(Au 20 nm) = 0.031 μmol/m^2, and ϕ(Au 80 nm, $(\mathbf{2})_{80}$) = 0.12 μmol/m^2, (c) $N(A\beta_{1-40}) = 8.4$ pmol, ϕ(Au 20 nm, $(\mathbf{2})_{20}$) = 0.15 μmol/m^2, and ϕ(Au 80 nm, $(\mathbf{3})_{80}$) = 0.59 μmol/m^2, (d) $N(A\beta_{1-40}) = 33.5$ pmol, ϕ(Au 20 nm, $(3)_{20}$) = 0.61 μmol/m^2, and ϕ(Au 80 nm, $(\mathbf{4})_{80}$) = 2.4 μmol/m^2, (e) $N(A\beta_{1-40}) = 167$ pmol, ϕ(Au 20 nm, $(\mathbf{4})_{20}$) = 3.1 μmol/m^2, and ϕ(Au 80 nm, $(\mathbf{5})_{80}$) = 12 μmol/m^2, and (f) $N(A\beta_{1-40}) = 700$ pmol, ϕ(Au 20 nm, $(\mathbf{5})_{20}$) = 12 μmol/m^2, and ϕ(Au 80 nm) = 47 μmol/m^2. The plots of θ versus ϕ are shown in Figure 2ii and exhibited a great match for both 20 nm and 80 nm gold, and the trend was best explained by the Langmuir−Freundlich model as[140]

$$\theta = \frac{(K_{LF}\phi)^{1/n}}{1 + (K_{LF}\phi)^{1/n}} \quad (2)$$

where K_{LF} is the Langmuir−Freundlich constant and n is a parameter characterizing the surface heterogeneity. To clarify the features observed around the region where θ values are increasing, the plot at $0 \le \phi \le 4$ μmol/m^2 is shown as an inset of Figure 2ii. The optimized K_{LF} and n values are listed in Table 1 with the reduced $-R^2$ values, $\langle R^2 \rangle$. The n value was ~0.37, and it confirmed that the adsorption that was taking place in the current system was heterogeneous. The observed trends of θ at $1.0 \ge \theta \gtrsim 0.8$ did not greatly match the Langmuir−Freundlich model. The analysis with the Langmuir model showed a Langmuir constant, K_L, of ~4×10^5 with $\langle R^2 \rangle \approx 0.86$. There is a modified version of the Langmuir−Freundlich equation

https://doi.org/10.1021/acs.langmuir.3c02923
Langmuir 2024, 40, 1728−1746

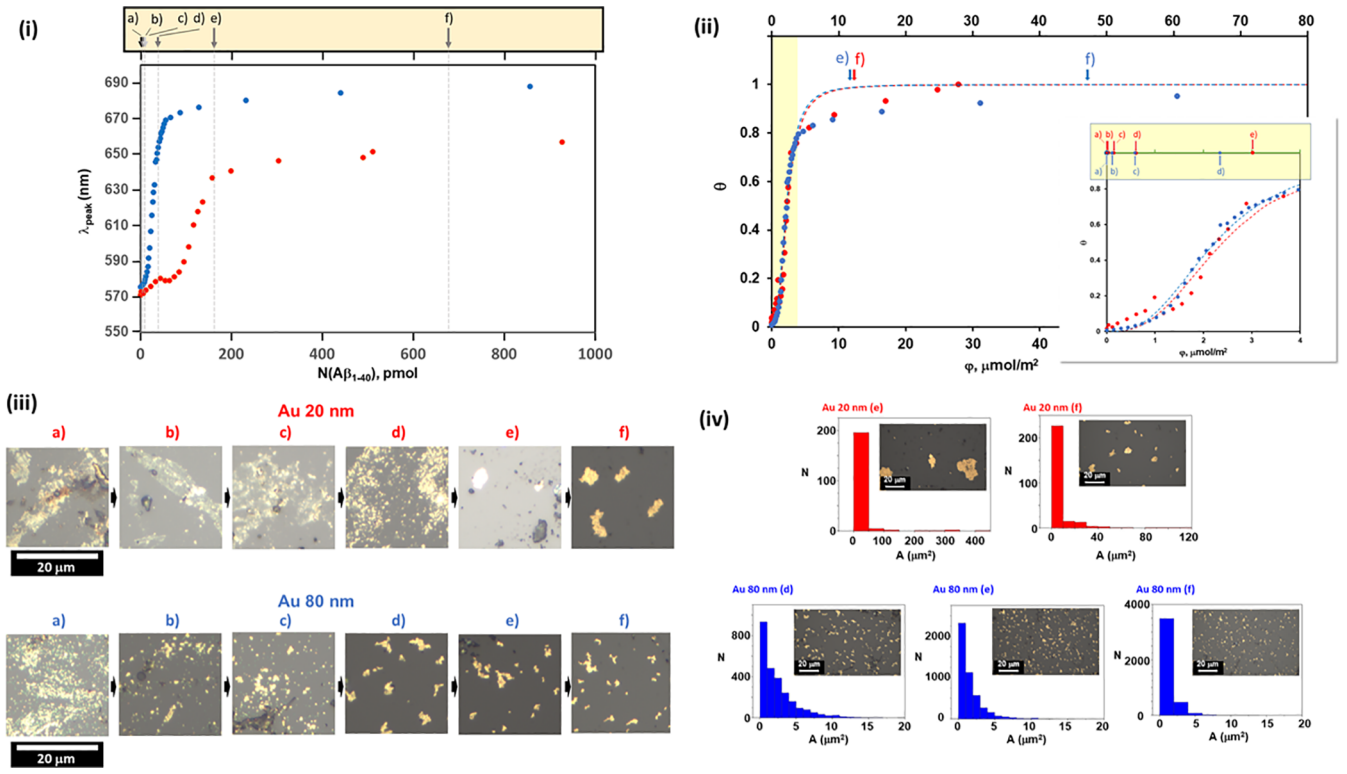

Figure 2. (i) Averaged SPR band peak, λ_{peak}, as a function of externally added Aβ_{1-40} (picomoles), N(Aβ_{1-40}), for 20 nm gold (red) and 80 nm gold (blue) colloids. The arrows (a−f) placed in the inserted box at the top show the location of each concentration corresponding to N(Aβ_{1-40}): (a) 0, (b) 1.7, (c) 8.4, (d) 33.5, (e) 167, and (f) 700 pmol. (ii) Coverage fraction, θ, defined in eq 2 plotted as a function of ϕ for 20 nm gold (red) and 80 nm gold (blue) colloids. The inset shows the plot in the region between $0 \leq \phi \leq 4$ μmol/m^2. The amounts of ϕ corresponding to N(Aβ_{1-40}) are marked in panels a−f in red for the 20 nm gold colloid and in blue for the 80 nm gold colloid. (iii) White-light images at the corresponding N(Aβ_{1-40}) labeled as panels a−f for 20 nm gold (red) and for 80 nm gold (blue). (iv) Histograms showing the distribution of the area of gold colloid aggregates and representative white-light images for 20 nm gold at (e) an N(Aβ_{1-40}) of 167 pmol and (f) an N(Aβ_{1-40}) of 700 pmol and for 80 nm gold at (d) an N(Aβ_{1-40}) of 33.5 pmol, (e) an N(Aβ_{1-40}) of 167 pmol, and (f) an N(Aβ_{1-40}) of 700 pmol.

Table 1. Parameters Extracted from the Langmuir−Freundlich Model Given in eq 2

d (nm)	K_{LF}	n	$\langle R^2 \rangle$
20	4.2(2) × 10^5	0.37(4)	0.968
80	4.46(8) × 10^5	0.37(2)	0.981

designed for adsorption from the liquid phase,[140,142] and the fit with that model exactly reproduced the values of K_{LF}, n, and $\langle R^2 \rangle$ listed in Table 1.

In a previous report, TEM images showed dispersed gold colloid particles under neutral or basic conditions (pH ∼10) and the formation of gold aggregates under acidic conditions (pH ∼4).[143] Here, we observed the formation of gold aggregates at high N(Aβ_{1-40}) values or under acidic (pH ∼3.7) conditions [white-light images at each N(Aβ_{1-40}) are shown in Figure 2iii]. There was a significant correlation between the stage of aggregation and ϕ. Comparing images between 20 and 80 nm gold around similar ϕ values showed a consistent morphology corresponding to a similar θ value. For example, the white-light image in Figure 2iii-e for 20 nm gold corresponds to an N(Aβ_{1-40}) of 167 pmol or a ϕ(Au 20 nm, $(4)_{20}$) of 3.1 μmol/m^2, which is similar to the white-light image of Figure 2iii-d [N(Aβ_{1-40}) = 33.5 pmol, and ϕ(Au 80 nm, $(4)_{80}$) = 2.4 μmol/m^2 for 80 nm gold].

We identified the clear morphology of aggregates at the two largest values of N(Aβ_{1-40}) (167 and 700 pmol) for 20 nm gold and the three highest values of N(Aβ_{1-40}) (33.5, 167, and 700 pmol) for 80 nm gold and extracted the average areas, A_a, of the aggregates by pixel analyses using ImageJ (Figure 2iv and Table 2). Interestingly, the A_a values of the aggregates originating from

Table 2. Averaged Areas (square micrometers) and Sampled Numbers of Gold Colloid Aggregates

d (nm)	N(Aβ_{1-40})	average area (μm^2)	sample number
20	167	12(50)	208
20	700	6(15)	268
30	33.5	2.5(26)	2553
30	167	1.6(18)	4669
30	700	1.1(13)	4085

20 nm gold were found to be significantly larger than those originating from 80 nm gold, and the average area was found to become smaller as ϕ increased for both 20 and 80 nm gold. This trend was more enhanced for 20 nm gold, which could be because the smaller surface area could allow for more networking among Aβ_{1-40} peptides adsorbed on the gold surface.

All white-light images were collected after samples were prepared on a disc after overnight water vaporization, as we interrogated the aggregation process related to N(Aβ_{1-40}) or ϕ rather than measuring aggregation over time. We did note that the value of θ was maintained at a consistent level overnight. For both 20 and 80 nm gold particles, there was no consistent morphology of the aggregates and no structured pattern or shape

https://doi.org/10.1021/acs.langmuir.3c02923
Langmuir 2024, 40, 1728−1746

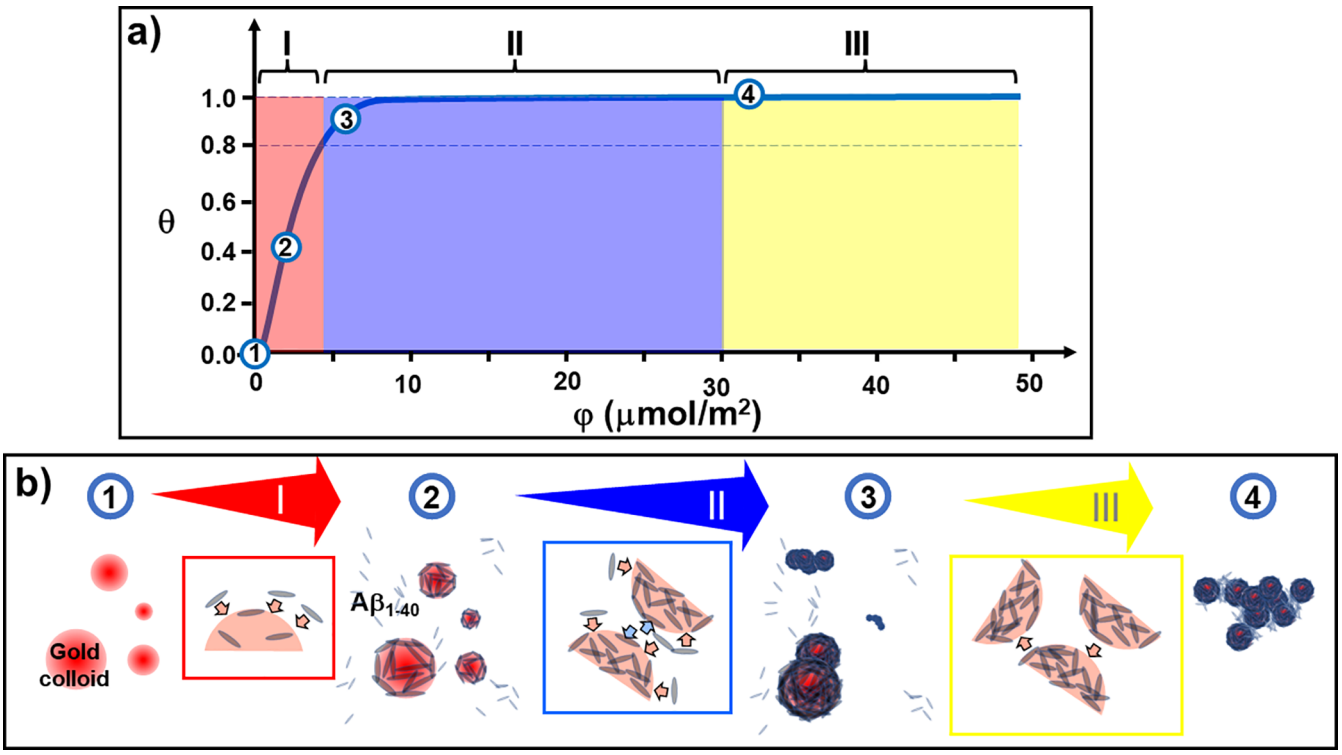

Figure 3. (a) Sketch of the plot of θ vs ϕ indicating four distinct spots (1−4) of the aggregation stages of I (induction of adsorption), II (continuation of adsorption and induction of protein−protein interaction), and III (continuation of adsorption and protein−protein interaction). The values of θ and ϕ roughly correspond to the experimental results. (b) Sketch of three progressive stages of the aggregation process of the spot corresponding to the plot shown in panel a.

was observed. We note this observation because it is possible that we are imaging an intermediate condition of the aggregation process. This intermediate condition is limited by the availability of Aβ_{1-40} involved in the aggregation process, which prevents it from proceeding to further aggregation. The conformation of Aβ_{1-40} contained in gold colloid aggregates, especially the conformation of Aβ_{1-40} at the interface of the gold colloid, may correspond to the oligomerization of dimers, which lead to fibrillogenesis in the development of AD. A significant match of characterization of θ for both 20 and 80 nm gold led us to construct a unified interpretation of the aggregation process as separated into stages I−III as well as four aggregation structures (Figure 3). In stage I (spot 1 to spot 2), the bare gold colloids (spot 1) start to contact Aβ_{1-40} molecules, which adsorb on the gold surface (spot 2), which corresponds to the range of $0 \leq \phi \leq 0.8$ [white-light images are shown in Figure 2iii for 20 nm gold (a) and 80 nm gold (a) for spot 1 and Figure 2iii for 20 nm gold (b−e) and Figure 2iii for 80 nm gold (b−d) for spot 2]. As a note, Aβ_{1-40} fibrils are shown as a simplified prolate shape in Figure 3, but we cannot determine their shape or network by white-light imaging. Stage II indicates the continuation of the adsorption of Aβ_{1-40} on the gold surface and growth of the aggregation through protein−protein interactions (spot 3), which corresponds to the white-light image of 20 nm gold (f) and 80 nm gold (e) (Figure 2iii). In stage II, significant discrepancies in the extracted θ values with respect to the simulation by the Langmuir−Freundlich model were observed. The Langmuir−Freundlich model is designed to describe the adsorption process, and stage II may involve protein−protein interactions that contribute to the aggregation process but do not affect adsorption, causing the observed value of θ to be lower than the value predicted by the model, which accounts for only adsorption (see Figure 2ii). In stage III, θ asymptotically reaches $\theta(\phi) = \theta_{max}$. Figure 3 shows where spot 4 is reached, which corresponds to the white-light image of 80 nm gold (f) in Figure 2iii. At this stage, adsorption of Aβ_{1-40} is terminated, and minor growth of the aggregates is expected.

SERS imaging was conducted for 20 and 80 nm gold at N(Aβ_{1-40}) values of 0, 1.7, 8.4, 33.5, 167, and 700 pmol. See Figure S1 for 20 nm gold and Figure S2 for 80 nm gold. As a representative SERS imaging map, 20 nm gold at an N(Aβ_{1-40}) of 700 pmol [ϕ(20 nm gold) = 12.3 μmol/m^2] and 80 nm gold at an N(Aβ_{1-40}) of 700 pmol [ϕ(80 nm gold) = 47.3 μmol/m^2] are presented with white-light images and components of the SERS spectrum (panels a and b, respectively, of Figure 4). All spectra were normalized against the maximum SERS signal of a given ϕ. For both 20 and 80 nm gold, the SERS signals were collected within the range of 200−2800 cm^{-1}. However, distinct spectral features were observed only within the range of 250−1800 cm^{-1}. In the examination of the SERS imaging [Figure 4a(iii),(iv),b(iii),(iv)], component A is a baseline and components B−D appear to share prominent features, indicating that the overall features of the peptides were consistent regardless of the location of the aggregate (each peak indicates a focal point being affected due to the nonflat surface of the aggregate sample). However, component D in the 80 nm gold sample [Figure 4b(iv)] exhibited more enhanced features in the range of ≤1000 cm^{-1}, indicating that the conformation of Aβ_{1-40} was inhomogeneous or possessed different degrees of interaction with the gold surfaces. It was also notable that the outline of the shape in the white-light image [Figure 4b(ii)] did not match that of the SERS image [Figure 4b(iii)]. The abrupt decreases in the SERS signals observed close to the starting range of the Raman shift (i.e., ∼100 cm^{-1})

https://doi.org/10.1021/acs.langmuir.3c02923
Langmuir 2024, 40, 1728−1746

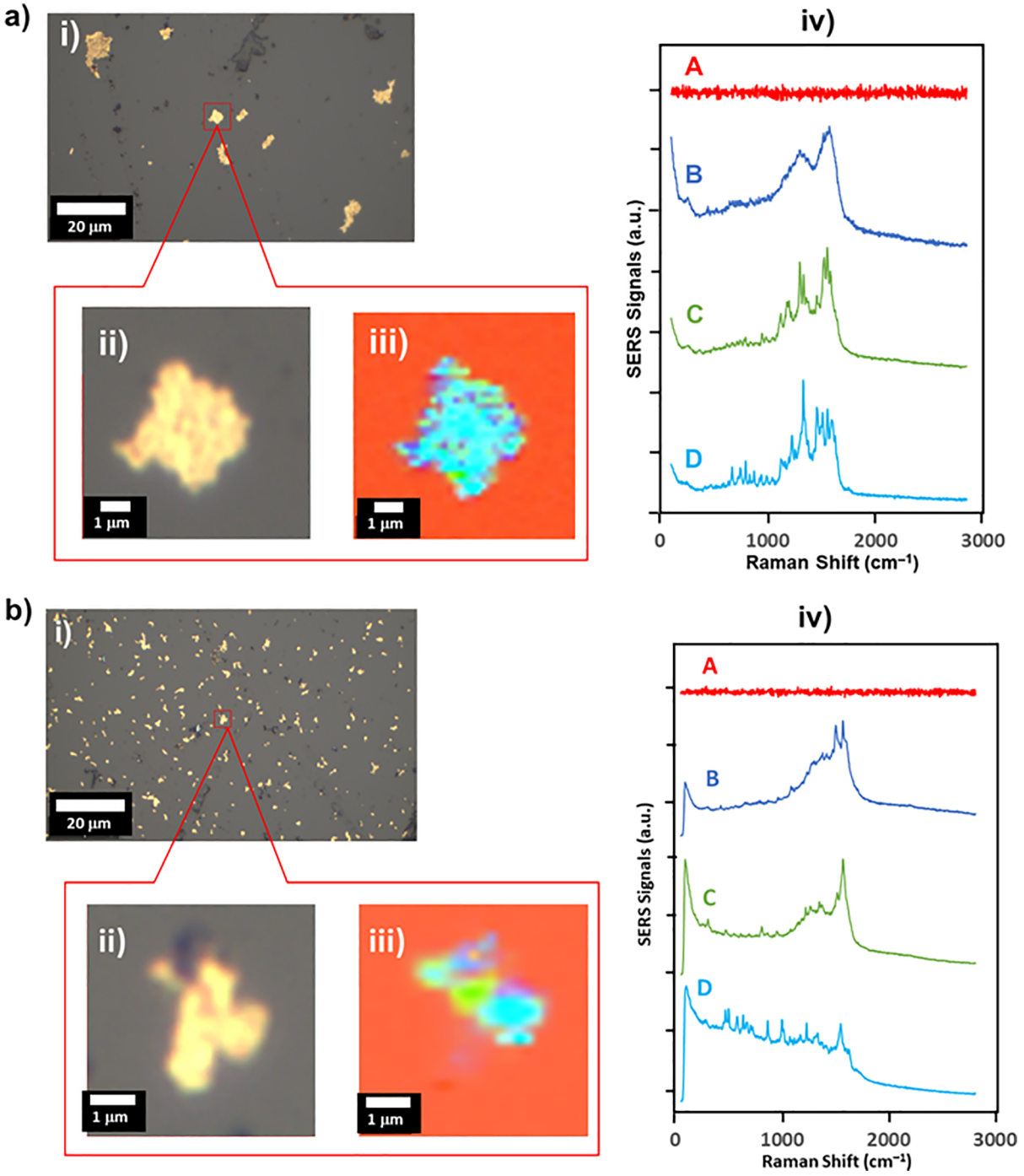

Figure 4. (a) Representative SERS spectrum imaging of 20 nm gold colloid aggregates for 700 pmol of Aβ_{1-40}. (i) White-light image, (ii) higher magnification of the white-light image marked by a red square, (iii) SERS image of components A−C shown in panel iv, and (iv) SERS spectra of components A−D. (b) Representative SERS spectrum imaging of 80 nm gold colloid aggregates for 700 pmol of Aβ_{1-40}. (i) White-light image, (ii) higher magnification of the white-light image marked by a red square, (iii) SERS image of components A−D shown in panel iv, and (iv) SERS spectra of components A−D.

were interpreted to be monitoring a cut profile by a notch filter of an excitation line. This was regarded as an artifact and was removed from the analysis. Because the aggregate surfaces must be composed of an inhomogeneous environment of protein−protein interactions, different degrees of gold−peptide interactions and peptide conformations will be detected. Typically, >200 SERS spectra are collected and examined to extract a representative SERS spectrum for a given ϕ, as shown in Figure 5a for 20 nm gold and Figure 5b for 80 nm gold. Here, $(\mathbf{1})_{20}$ = ϕ(Au 20 nm) = 0.0 μmol/m^2, $(\mathbf{2})_{20}$ = ϕ(Au 20 nm) = 0.15 μmol/m^2, $(\mathbf{3})_{20}$ = ϕ(Au 20 nm) = 0.61 μmol/m^2, $(\mathbf{4})_{20}$ = ϕ(Au 20 nm) = 3.1 μmol/m^2, ϕ(Au 20 nm, $(\mathbf{5})_{20}$) = 12.3 μmol/m^2, $(\mathbf{1})_{80}$ = ϕ(Au 80 nm) = 0.0 μmol/m^2, $(\mathbf{2})_{80}$ = ϕ(Au 80 nm) = 0.12 μmol/m^2, $(\mathbf{3})_{80}$ = ϕ(Au 80 nm) = 0.59 μmol/m^2, $(\mathbf{4})_{80}$ = ϕ(Au 80 nm) = 2.4 μmol/m^2, and $(\mathbf{5})_{80}$ = ϕ(Au 80 nm) = 11.8 μmol/m^2. Each number (**1**−**5**) in Figure 5 corresponds to a similar value for 20 and 80 nm gold to make a clear comparison [e.g., ϕ at $(\mathbf{2})_{20}$ ≈ ϕ at $(\mathbf{2})_{80}$]. The location of each

https://doi.org/10.1021/acs.langmuir.3c02923
Langmuir 2024, 40, 1728−1746

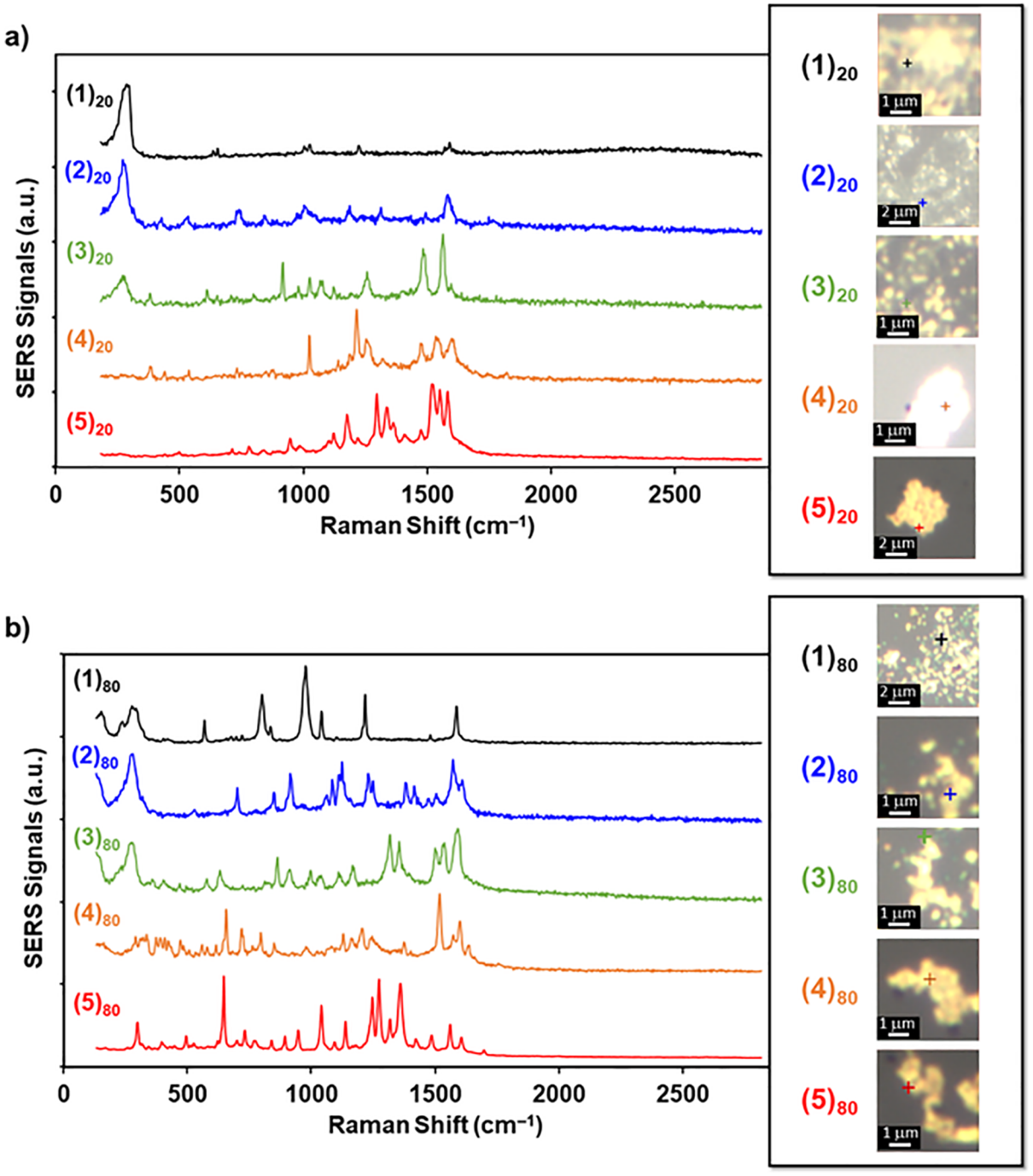

Figure 5. (a) SERS spectra of 20 nm gold colloid aggregates for each concentration of Aβ_{1-40}: $(\mathbf{1})_{20}$, $\phi = 0$ μmol/m^2; $(\mathbf{2})_{20}$, $\phi = 0.15$ μmol/m^2; $(\mathbf{3})_{20}$, $\phi = 0.61$ μmol/m^2; $(\mathbf{4})_{20}$, $\phi = 3.07$ μmol/m^2; and $(\mathbf{5})_{20}$, $\phi = 12.3$ μmol/m^2. The white-light images at the corresponding ϕ values are shown in the right insets. (b) SERS spectra of 80 nm gold colloid aggregates for each concentration of Aβ_{1-40}: $(\mathbf{1})_{80}$, $\phi = 0$ μmol/m^2; $(\mathbf{2})_{80}$, $\phi = 0.12$ μmol/m^2; $(\mathbf{3})_{80}$, $\phi = 0.59$ μmol/m^2; $(\mathbf{4})_{80}$, $\phi = 2.4$ μmol/m^2; and $(\mathbf{5})_{80}$, $\phi = 11.8$ μmol/m^2. The white-light images at the corresponding spectrum are shown in the right insets.

representative SERS spectrum was collected and is marked with a plus sign in the corresponding white-light image on the right inset box.

For 20 nm gold, the most remarkable feature was that a Raman shift of ~275 ± 9 cm^{-1} (peak α) appeared prominently from $(\mathbf{1})_{20}$ $\phi = 0$ μmol/m^2 to $(\mathbf{3})_{20}$ $\phi = 0.613$ μmol/m^2, with a decrease in its intensity as ϕ increased. This trend also corresponds to the morphology changing from a cluster of particles to the formation of an aggregate. We note that at higher ϕ values, the disappearance of peak α corresponded to the appearance of peaks between ~800 and ~1600 cm^{-1}, which were mainly assigned as amide I–III bands (see Table 3i, Table S1-I, and Table S2). Thus, peak α appears to be enhanced by bare gold surfaces at pH ~3.7 and diminished by the coverage of the gold surface by Aβ_{1-40}. We previously reported that peak α did not appear at pH ≤7. Gao et al. reported the Au–Cl$^-$ mode at 275 cm^{-1} under 500 mV of potential was applied on the gold electrode.[144] Because we used hydrochloric acid to create an acidic condition (pH ~3.7), peak α may originate from the Au–Cl$^-$ mode. However, peak α was not observed at pH ≥7 and was

https://doi.org/10.1021/acs.langmuir.3c02923
Langmuir 2024, 40, 1728–1746

Table 3. List of Raman Shifts ($\tilde{\nu}_{Raman}$) of SERS Spectra for Gold Colloid Aggregates of 20 nm Gold (i) and 80 nm Gold (ii) after Insertion of 700 pmol of A$\beta_{1\text{-}40}$ or ϕ(20 nm gold) = 12.3 μmol/m^2 and ϕ(80 nm gold) = 47.3 μmol/m^2[a]

Sequence of A$\beta_{1\text{-}40}$
NH_2-DAEFRHDSG[10]YEVHHQKLVF[20]FAEDVGSNKG[30]A I I GLMVGGV[40]V-COOH

The labeling for the β strand for β sheet are: **β1: 17 – 21** and **β2: 29 – 40**.[152]
The sequences appear in both **β1 and β2** are: L, A, and V.

(i)

$\tilde{\nu}_{Raman}$	Assignment
498.3	S-S str. [155-159]
716.6	COO^- def., Backbone, (**F-G-F-G**), str. C-S[155-156, 159-161]
745.3	Citrate anion on gold surface – CC str. of bidendate coordination (t_2) of terminal group of citrate[162]
778.3	Citrate anion on gold surface – CC str. of bidendate coordination (t_2) of terminal group of citrate[162]
835.7	Y,[163-166] C-C str. (**I – G – G**, L- **G**, I)[160]
875.3	C-C str. (**G - G - F**, **F - G - F - G**, M),[160] Y,[155, 157]
946.1	C-C str. (I - **G**, Y),[160] CN str., ring def. (H)[147, 160]
987.8	C-C str., β-sheet or Phe(**F**),[167] Citrate anion on gold surface – CC str. terminal carboxylate [162]
1100.3	C-N str. (A-A, A-I-A-I)[160]
1122.0	C-C_α and C-N str. (A or I)[163-167] NH_3^+ def. (I-**G-G**)[160]
1176.7	side-chain (Y),[147] C-H str. (Y),[155-156] Amide III[168]
1217.1	Amide III (β-sheets)[147]
1296.2	$\nu_{Au\text{-}citrate}$ C-O-Au str. mono-dendate binding of terminal carboxylates (by Cl^-),[162] Amide III, C-H, C-C,[155, 159, 169]
1336.7	CH_2 wag (**G**, Y),[160] C-H def. (Y)[155-156, 160] CH_3, CH_2 bend[147]
1361.2	CH_3 sym. def. (A)[155, 158, 160]
1413.4	COO^- sym. str., Backbone (Q, **G**-I, **G-G-F**, **F-G-F-G**)[160]
1475.1	CH_3 asym. bend (A-A)[160]
1520.6	Amide II (anti-parallel β-sheets)[147]
1550.7	Citrate anion on gold surface - coordinated terminal carboxylates[162]
1582.2	COO^- asym. str. Backbone (**F-G-F-G**), Ring CC str. (**F**)[160], Ring CC str. (**F**), R- COO^--Au str., $\nu_{a\text{-}citrate}$ (COO^-), benzene ring def. or str., Amide II, C=C str. (**F**, Y)[147, 155, 158, 160, 162-166, 169-171]

https://doi.org/10.1021/acs.langmuir.3c02923
Langmuir 2024, 40, 1728−1746

Table 3. continued

(ii)

$\tilde{\nu}_{Raman}$	Assignment
257.5	Unassigned
277.5*	Au_n[145-146]
296.0[⊕]	$R_2Au(SCN)_4$ (R = $(CH_3)_4N^+$ or $(C_2H_5)_4N^+$), Au-N in $LAuCl_3$[151]
315.2[⊕]	(2, 4-lut) $AuCl_3$, Me_3PAuCl, Et_3PAuCl, Me_2SAuCl, $Me_3AsAuCl$[151]
328.5[⊕]	φ_3PAuCl, Me_2SAuCl[151]
366.2[⊕]	planar-trans $AuCl_2(PZ_3)_2$, $AuCl_2(PZ_3)_2$, asym. str. $PyAuCl_3$, asym. str. (2-MePy)$AuCl_3$, asym. str. (3-MePy)$AuCl_3$, asym. str. (4-MePy)$AuCl_3$, asym. str. (2, 6 -lut), asym. str. (3, 5 -lut) $AuCl_3$, asym. str. (2, 4-lut) $AuCl_3$, asym. str. (4-CNPy)$AuCl_3$, asym. str. (Py-d_5)$AuCl_3$[151]
379.5[⊕]	planar trans $AuCl_2(PZ_3)_2$, $AuCl_2(PZ_3)_2$[151]
397.3[⊕]	planar trans $AuCl_2(PZ_3)_2$, $AuCl_2(PZ_3)_2$[151]
424.4[⊕]	Au-N in $[\varphi_4As][Au(N_3)_4]$[151]
455.0	C-S str.[155-156]
463.8	C-S str.[155]
481.6	Unassigned
501.6	S-S str.[155-159]
526.1	N-H def., S-S str., skeletal, def.[155, 158-159, 161, 169]
572.5	C-C str., S-S str.[155, 167]
608.0	ring def. (Y, F)[147] C-S str. (Y), COO^- wag, Backbone, COO^- wag ([illegible] – G – G, G –[illegible], [illegible] –[illegible] –[illegible], [illegible] –[illegible], F)[155-156, 160, 163-166]
621.4	COO^- wag + ring C-C twist (G – G – F, F – G – F – G), COO^- wag + ring C-C twist (F G – G -F)[160]
648.0	C-S str. (Y),[155-156, 159, 161] COO^- bend or C-S str. (Y) [170-171]
656.9	Unassigned
670.2	Unassigned
690.1	C-C, C-O bend[155]
708.2	sulfoxide (M)[163-166] C-S str., COO^- def.,[155-156, 159, 161, 169] COO^- in-plane def. (Q, D)[147]
727.8	COO^- def., Backbone, COO^- def. ([illegible] –[illegible] –[illegible]), COO^- def. (F- G – G -F, [illegible] – G)[160]
745.1	Citrate anion on gold surface –CC str. of bidendate coordination (t_2) of terminal group of citrate[162]
785.5	Citrate anion on gold surface –CC str. of bidendate coordination (t_2) of terminal group of citrate[162]
798.8	C-H str., -N-H def.[155-156]
812.1	ring breathing (Y) [147]
832.1	Y,[163-166] C-C str. ([illegible] – G – G, L- G, [illegible])[160]
845.5	Y ([illegible], [illegible] – G, G –[illegible])[160]
869.8	C-C str. (G – G – F, F – G -F- G),[160] Y,[155, 157] C-C str. (M)[160]
896.4	C-C str. ([illegible] –[illegible] –[illegible], [illegible] –[illegible], Q) [160]
918.6	C-C str. (G –[illegible], [illegible] – G – G), C-COO^- str. ([illegible] –[illegible] –[illegible] –[illegible], [illegible] –[illegible] –[illegible]) [160]
947.5	C-C str. ([illegible] - G, Y),[160] CN str., ring def. (H)[147, 160]
975.3	C-COO^- str. (Q, D)[147], $\nu_{Citrate}$ C_2-t_2[162]
994.1	$\nu_{Citrate}$ (CC) C_2-t_2t_2,[162] benzene ring breathing[155-157, 159, 169]
1028.1	C-H in-plane (F), in-plane ring CH def. (F – G – G – F, F) [160, 163-166, 170-171]
1093.6	C-C str., C-N str. [155-156, 160, 169]
1147.1	NH_3^+ def. ([illegible] – G – G), Backbone[160]
1169.3	Y, F,[155-156, 163-166] Y (side chain),[147] NH^+ def.[160]
1193.7	Unassigned
1224.8	Amide III[160]
1258.0	Amide III disordered,[163] CH_2 wag ([illegible] – G – G, G –[illegible])[160]
1302.4	$\nu_{Au\text{-}citrate}$ C-O-Au str. mono-dendate binding of terminal carboxylates (possibly by Cl^-)[162] CH_2 wag ([illegible], Q), CH def. Leu([illegible])[160]
1311.8	CH_2 wag (Q, G –[illegible], F – G – F – G, G – G – F) [160]
1335.7	CH_2 wag (G, Y),[160] C-H def. (Y)[155-156, 160] CH_3 bend, CH_2 bend[147]
1366.0	CH_3 sym. def. ([illegible])[155, 158, 160]
1417.5	COO^- sym. str., backbone (Q, G -[illegible], G - G - F, F - G - F - G)[160]
1446.6	CH_2 sciss. (G, Q, F – G – G – F, G – G – F, F – G -F- G),[160, 167, 170] def. of CH_2/CH_3 (F – G – F – G),[155, 159-160, 163-166, 170] CH_2 bend. (F)[160, 167, 172]
1481.9	Amide II[168]
1508.7	Amide I, benzene ring str.,[155, 157, 169] C-H str., F, H[160]
1541.4	$\nu_{Au\text{-}citrate}$ coordinated terminal carboxylates[162]
1570.0	Amide II[147]
1588.6	Ring CC str. (F), R- COO^--Au str., $va_{Citrate}$ (COO^-), benzene ring def. or str., Amide II, C=C str. (F, Y),[147, 155, 158, 160, 162-166, 169-171] COO^- asym. str. Backbone (F-G-F-G), Ring CC str. (F)[160]
1609.3	C=C bend (Y, F),[170-171] ring CC Sym. Stretch (Y)[160]
1648.5	Amide I (F - G - F - G, L- G - G, G - G - F, [illegible] -[illegible] -[illegible] -[illegible]), α-helix and random coil[160, 168]
2225.3	Unassigned

https://doi.org/10.1021/acs.langmuir.3c02923
Langmuir 2024, 40, 1728−1746

Table 3. continued

(iii)

$\tilde{\nu}_{Raman}$	d(Au)	Assignment
498.3	20	S-S str.[155-159]
501.6	80	S-S str.[155-159]
716.6	20	COO^- def., Backbone, (F - G - F - G), str. C-S[155-156, 159-161]
727.8	80	COO^- def. ([illegible] - [illegible] - [illegible], F - G - G - F, [illegible] - G) Backbone[160]
745.3	20	$\nu_{Au\text{-}citrate}$ CC str. of bidendate coordination (t_2) of terminal group of citrate[162]
745.1	80	$\nu_{Au\text{-}citrate}$ CC str. of bidendate coordination (t_2) of terminal group of citrate[162]
778.3	20	$\nu_{Au\text{-}citrate}$ CC str. of bidendate coordination (t_2) of terminal group of citrate[162]
785.5	80	$\nu_{Au\text{-}citrate}$ CC str. of bidendate coordination (t_2) of terminal group of citrate[162]
835.7	20	Y,[163-166] C-C str. ([illegible] – G – G, L- G, [illegible])[160]
832.1	80	Y,[163-166] C-C str. ([illegible] – G – G, L- G, [illegible])[160]
875.3	20	C-C str. (G - G - F, F - G - F - G, M),[160] Y,[155, 157]
869.8	80	C-C str. (G - G - F, F - G - F - G, M),[160] Y,[155, 157]
946.1	20	C-C str. ([illegible] - G, Y),[160] CN str., ring def. (H)[147, 160]
947.5	80	C-C str. ([illegible] - G, Y),[160] CN str., ring def. (H)[147, 160]
987.8	20	C-C str., β-sheet or Phe(F),[167], $\nu_{Au\text{-}citrate}$ CC str. terminal carboxylate, joint vibration of modes in c_2-t_2t_2 and c_2t_2-t_2, spanning of the nano-gap with modes c_2-t_2t_2 and c_2-t_2, chloride – salted aggregates gap spanning mode c_2-t_2t_2 [162]
994.1	80	$\nu_{Au\text{-}citrate}$ joint vibration of modes in c_2-t_2t_2 and c_2t_2-t_2, spanning of the nano-gap with modes c_2-t_2t_2 and c_2-t_2, chloride – salted aggregates gap spanning mode c_2-t_2t_2[162] benzene ring breathing[155-157, 159, 169]
1100.3	20	C-N str. ([illegible] - [illegible], [illegible] - [illegible] - [illegible] - [illegible])[160]
1093.6	80	C-C str., C-N str.[155-156, 160, 169]
1176.7	20	side-chain (Y),[147] C-H str. (Y),[155-156] Amide III[168]
1169.3	80	Y, F,[155-156, 163-166] Y (side chain),[147] NH^+ def.[160]
1296.2	20	Amide III, C-H, C-C,[155, 159, 169] $\nu_{Au\text{-}citrate}$ C-O-Au str. mono-dendate binding of terminal carboxylates (by Cl^-)[162]
1302.4	80	CH_2 wag ([illegible], Q), CH def. Leu([illegible]),[160] $\nu_{Au\text{-}citrate}$ C-O-Au str. mono-dendate binding of terminal carboxylates (by Cl^-)[162]
1336.7	20	CH_2 wag (G, Y),[160] C-H def. (Y)[155-156, 160] CH_3, CH_2 bend[147]
1335.7	80	CH_2 wag (G, Y),[160] C-H def. (Y)[155-156, 160] CH_3, CH_2 bend[147]
1361.2	20	CH_3 sym. def. ([illegible])[155, 158, 160]
1366.0	80	CH_3 sym. def. ([illegible])[155, 158, 160]
1413.4	20	COO^- sym. str., backbone (Q, G - [illegible], G - G - F, F - G - F - G)[160]
1417.5	80	COO^- sym. str., backbone (Q, G - [illegible], G - G - F, F - G - F - G)[160]
1550.7	20	$\nu_{Au\text{-}citrate}$ coordinated terminal carboxylates[162]
1541.4	80	$\nu_{Au\text{-}citrate}$ coordinated terminal carboxylates[162]
1582.2	20	COO^- asym. str. backbone (F - G - F - G), Ring CC str. (F),[160] Ring CC str. (F), benzene ring def. or str., Amide II, C=C str. (F, Y),[147, 155, 158, 160, 162-166, 169-171] $\nu_{Au\text{-}citrate}$ central carboxylates, COO^- str., asym. str. ν_a (COO) of carboxylate - Au[162]
1588.6	80	COO^- asym. str. backbone (F - G - F - G), Ring CC str. (F),[160] Ring CC str. (F), benzene ring def. or str., Amide II, C=C str. (F, Y),[147, 155, 158, 160, 163-166, 169-171] $\nu_{Au\text{-}citrate}$ central carboxylates, COO^- str., asym. str. ν_a (COO) of carboxylate - Au[162]

[a]The common modes observed in sections i and ii are summarized in section iii. The assignment marked with an asterisk was proposed by this work on the basis of the DF-TB calculation,[145,146] and the assignments marked with a ⊕ were nonconclusively suggested as gold−ligand modes referenced from the study by Ferraro.[151] The modes shown with bold fonts in sections i and ii indicate those not identified as common modes in section iii. Abbreviations: def., deformation; str., stretching; sym., symmetric; asym., asymmetric, $\nu_{Citrate}$, mode associated with the citrate; d(Au), diameter of a gold nanoparticle. Amino acid abbreviations: Y, tyrosine; L, leucine; G, glycine; A, alanine; M, methionine; F, phenylalanine; Q, glutamine; K, lysine; R, arginine; N, asparagine; V, valine; I, isoleucine; E, glutamic acid; H, histidine (see Table S2).

still observed when an acidic condition (pH ∼4) was created with H_2SO_4. Thus, peak α is considered to be the mode that engages the gold colloidal surfaces. On the basis of the values reported with the density functional tight-binding approach, one of the normal modes of neutral gold clusters ($Au_{n=5,\ 6,\ 12,\ 16,\ 20,\ or\ 58}$) appears around 275 cm^{-1}.[145,146]

The data collected for 80 nm gold resembled those for 20 nm gold, as peak α at 276 ± 9 cm^{-1} appeared prominently when $(\mathbf{1})_{80}$ ϕ = 0 μmol/m^2, $(\mathbf{2})_{80}$ ϕ = 0.12 μmol/m^2, and $(\mathbf{3})_{80}$ ϕ = 0.59 μmol/m^2 (see Figure 5). We note the signs of morphology change at $(\mathbf{4})_{80}$ ϕ = 2.4 μmol/m^2 indicating that peak α was not present when the features between ∼800 and 1600 cm^{-1} were observed and that the assignment of peak α is likely $Au_{n=5,\ 6,\ 15,\ 16,\ 20,\ or\ 58}$,[145,146] the same as that of 20 nm gold. We attempted to assign the modes observed for ϕ = 0 μmol/m^2 with citrate; however, all modes observed below 850 cm^{-1} were not identified (Table 3ii, Table S1-II, and Table S2). The spectral lines ranging between ∼800 and ∼1600 cm^{-1} observed for 80 nm gold as ϕ increased resembled those observed for 20 nm gold (see Figure 5b). However, in contrast to the spectral features observed for 20 nm gold, spectral lines ranging between ∼350 and ∼800 cm^{-1} for 80 nm gold appeared as ϕ increased. To clarify the differences and similarities of the spectral features and to make plausible assignments, the spectral lines observed at the highest $N(A\beta_{1-40})$ of 700 pmol [i.e., ϕ(20 nm gold) = 12.3 μmol/m^2, and ϕ(80 nm gold) = 47.3 μmol/m^2] are listed in Table 3 for (i) only 20 nm gold and (ii) only 80 nm gold; also shown are (iii) common spectral lines for both 20 and 80 nm gold. The spectral features between ∼800 and ∼1600 cm^{-1} that appeared in both 20 and 80 nm gold (see Table 3iii) are considered to be associated with amino acids over the gold surface forming amide I−III bands, which are affected by interactions such as C−N/C−C_α/C−H stretching, NH_3^+/C−H deformation, CH_2 wag/deformation, CH_3 symmetric deformation, CH_3 asymmetric bending, COO^- symmetric/asymmetric stretching, and ring C−C stretching. Additional features that may be associated with amino acids appeared in the spectra below 1000 cm^{-1}, and they were assigned as C−C/C−S/C−N stretching or COO^-/ring deformation. As a notable band may be associated with the β-pleated sheet conformation, the feature associated with amide II, random coil fibril, core β-sheet (1534−1569 cm^{-1})[147] was observed for both 20 nm gold (1550.7 cm^{-1})

https://doi.org/10.1021/acs.langmuir.3c02923
Langmuir 2024, 40, 1728−1746

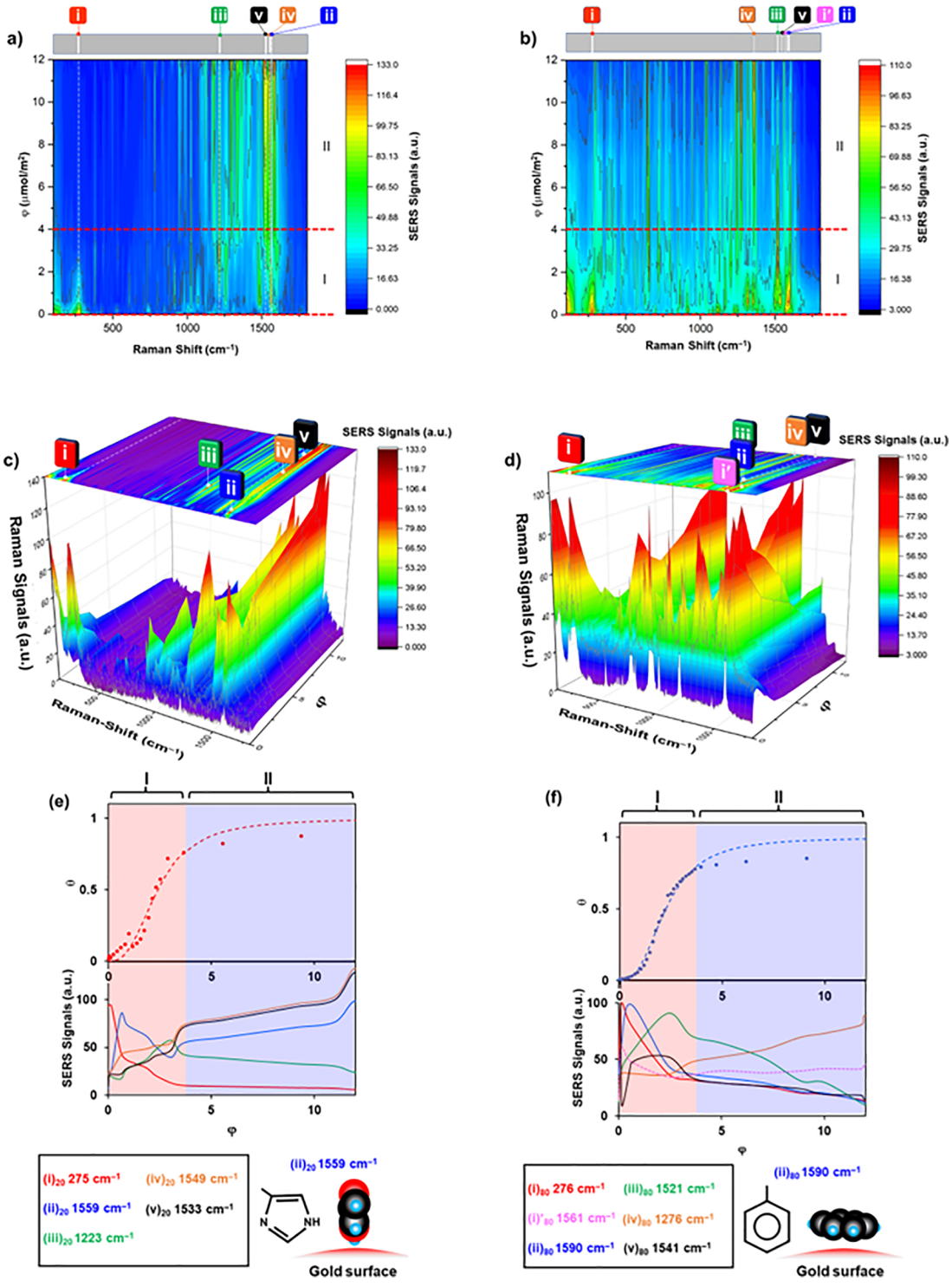

Figure 6. (a) SERS spectrum contour map for 20 nm gold with five marked spectral line positions: $(i)_{20}$ 275 cm^{-1}, $(ii)_{20}$ 1559 cm^{-1}, $(iii)_{20}$ 1223 cm^{-1}, $(iv)_{20}$ 1549 cm^{-1}, and $(v)_{20}$ 1533 cm^{-1}. (b) SERS spectrum contour map for 80 nm gold with six marked spectral line positions: $(i)_{80}$ 276 cm^{-1}, $(i)'_{80}$ 1561 cm^{-1}, $(ii)_{80}$ 1590 cm^{-1}, $(iii)_{80}$ 1521 cm^{-1}, $(iv)_{80}$ 1276 cm^{-1}, and $(v)_{80}$ 1541 cm^{-1}. (c) Three-dimensional (3D) map of the SERS spectrum as a function of ϕ ($0 \leq \phi \leq 12$ $\mu mol/m^2$) for 20 nm gold with a contour map on the top. The positions of each representative mode type explained in panel a are also indicated. (d) 3D map of the SERS spectrum as a function of ϕ ($0 \leq \phi \leq 12$ $\mu mol/m^2$) for 80 nm gold with a contour map on the top. The positions of each representative mode type explained in panel b are also indicated. (e) Plot of θ vs ϕ (top) reproduced from Figure 2ii for 20 nm gold for $0 \leq \phi \leq 12$ $\mu mol/m^2$. The corresponding aggregation stages explained in Figure 3 are also shown. SERS signals plotted as a function of ϕ for the representative modes explained in panel a (bottom). The right bottom shows a sketch of the suggested initial adsorption process at the 20 nm gold surface where histidine NH or C═C bonds are approaching. (f) Plot of θ vs ϕ (top) reproduced from Figure 2ii for 80 nm gold for $0 \leq \phi \leq 12$ $\mu mol/m^2$. The corresponding aggregation stages explained in Figure 3 are also shown. SERS signals plotted as a function of ϕ for the representative modes explained in panel b (bottom). The right bottom shows a sketch of the suggested initial adsorption process at the 80 nm gold surface where a plane of a benzene ring of tyrosine or phenylalanine is making contact.

https://doi.org/10.1021/acs.langmuir.3c02923
Langmuir 2024, 40, 1728−1746

and 80 nm gold (1541.4 cm^{-1}). There are modes associated with interactions with the gold surface, and they can originate from a segment of amino acids or a specific oligomer being formed at or attracted to the gold interface; however, they have not been reported in studies of Aβ fibrils. As a prominent difference from 20 nm gold, 80 nm gold showed modes ranging below ~800 cm^{-1} with relatively high densities in addition to those ranging between ~800 and 1600 cm^{-1}. Several modes below 450 cm^{-1} were not assigned and may indicate the specific modes unique to the sample condition developed in this work, such as interactions between the gold surface and amino acids. The origin of the difference in sensitivity of 20 and 80 nm gold for the modes ranging between ~250 and ~800 cm^{-1} is likely to be dependent on the nanosize. First, we considered a nanosize dependence to a sensitivity for particular modes. Although no detailed studies have been performed to explore surface roughness as a function of colloid diameter, the surface roughness has been crucial for enhancing SERS signals due to heterogeneous nanoscale height variation.[148,149] Defining the surface roughness as a stochastic height variation to the smooth surface of an ideal nanoparticle,[150] we found the surface roughness must be equal assuming that the surface homogeneously consisted of gold atoms. Second, we took into account the fact that physical size affects the surface condition for adsorption. Our study reports newly observed Raman shifts in the range of ~250−500 cm^{-1}. Up to this point, the available assigned Raman modes on Aβ_{1-40} are limited to 500 cm^{-1} for the lower-frequency range. A significant amount of gold metal−ligand modes were reported in the range of 250−600 cm^{-1}.[151] Thus, nonconclusive and suggestive assignments can be made for those lines associated with the gold metal surface. Those lines are marked with a $\oplus$ with temporal assignments in Table 3, Table S1, and Table S3. We simulated the surface coverage (Θ, which corresponds to θ_{max} in eq 1) of gold colloids by amyloidogenic peptides[141] and found that Θ(20 nm gold) = 0.74 and Θ(80 nm gold) = 0.77. While 80 nm gold was estimated to have a higher coverage compared to that of 20 nm gold, the simple spherical approximation of the colloid shows 80 nm gold provides an open area of ~1.5×10^4 nm^2 by a bare gold colloid surface and that of 20 nm gold will be 900 nm^2. Thus, it is plausible that those unassigned modes are associated with bonding between the gold surface and a segment of Aβ_{1-40} responsible for adsorption but not the part for protein−protein interaction. One of the focal points of this study is to identify the modes associated with adsorption and aggregation.

We formed a spectral line group for 20 and 80 nm gold as a function of ϕ under the equivalent assignment of the mode at different aggregation stages summarized in Table S3. Then, representative modes were marked on the top of a contour map in panels a and c of Figure 6 for 20 nm gold (i−v) and panels b and d of Figure 6 for 80 nm gold (i, i′, and ii−v). The line group was identified using a filtering range of ±10 cm^{-1}, and this filter range was termed a deviation of ±9 cm^{-1} of the peak around 275 cm^{-1} in this work. Then, we made line assignments within each line group to the best matched reported assignments. In some cases, to be consistent with the assignment of each line group, lines positioned beyond the filter range (±10 cm^{-1}) needed to be chosen. To hypothesize a plausible mechanism of the involvement of particular sequences of Aβ_{1-40} in the peptide−peptide interactions at the interface, we attempted to correlate the modes with particular sequences (Table 3). Utilizing the labeling of β1 (Aβ_{7-21}) and β2 (Aβ_{29-40}),[152] the SERS spectra at the highest aggregation stage, where N(Aβ_{1-40}) = 700 pmol, were analyzed (see Table 3i−iii). A significant number of modes associated with alanine (Ala or A) β1, phenylalanine (Phe or F) β1, leucine (Leu or L) β1 and β2, and glycine (Gly or G) β1 and β2 were found.

To understand and correlate the possible modes or particular sequences of Aβ_{1-40} with respect to aggregation stages I−III shown in Figure 3, we have categorized the following five types of modes (i−v) as sketched in Figure S3.

> For type i, a particular mode appeared at ϕ = 0 and disappeared within an early stage I. If the SERS signals were negligible at ϕ = 0 but still exhibited a feature of type i, it was labeled as type (i)′.
>
> For type ii, the mode possessed maximum SERS signals around ϕ ~ 0.5 (i.e., early stage I).
>
> For type iii, the modes possessed maximum SERS signals during the later stage I.
>
> For type iv, the modes start to appear or grew more during stage II.
>
> For type v, the modes start to appear or grew more during the later stage II or stage III.

Among all observed modes, prominent modes were selected and sorted into types i−v. First focusing on the region of stage I and the early stage II (corresponding to $0 \le \phi \le 12$ μmol/m^2), we found remarkable differences between 20 and 80 nm gold as seen in the contour map and 3D SERS signals shown in panels a and c of Figure 6 for 20 nm gold and in panels b and d of Figure 6 for 80 nm gold. To simplify and clarify the feature, the most prominent SERS modes of each type (i−v) were picked and labeled as a representative mode for each, as shown in panels a−d of Figure 6. In panels e and f of Figure 6, the trends of the SERS signal as a function of ϕ are plotted for each representative mode of each type with the plot of θ versus ϕ reproduced from Figure 2ii. While sharper peak maxima were observed in panels e and f of Figure 6, these were likely due to the limited spectral observation points and do not necessarily represent the actual curvature. The full list and assignments of spectral lines used in this analysis are summarized in Table S3 and labeled in the contour maps in Figures S4, S5, S6a, and S6b.

For 20 nm gold, at the initial stage I, a representative type i mode [$(i)_{20}$ 275 cm^{-1}] was assigned as the vibrational mode of gold clusters ($Au_{n=5, 6, 15, 16, 20, or 58}$). As increased during early stage I, which must be associated with an induction of adsorption, the type ii mode [$(ii)_{20}$ 1559 cm^{-1}] was prominently observed. This mode was considered to be carboxylate interacting on the gold surface (i.e., −COO−Au), and no particular sequence was identified to be responsible for the adsorption. However, although the intensity was not as prominent as that of mode $(ii)_{20}$, the other type ii mode with significant intensity at 1485 cm^{-1} associated with histidine (His or H) NH deformation or C═C asymmetric stretching was observed, implying the possible involvement of 6His, 13His, or 14His for the first approach of the adsorption. Then, stage I was followed by the type iii mode [$(iii)_{20}$ 1223 cm^{-1}], considered to be CH_2 wag in 33Gly-34Leu. Then, during stage II, where a continuation of adsorption and induction of protein−protein interaction may be taking place, the type iv mode [$(iv)_{20}$ 1549 cm^{-1}] clearly grew, and it showed the involvement of random coils, fibrils, or core β-sheets. Two other type iv modes at 1312 cm^{-1} (CH_2 wag in F-G-F-G or G-G-F) and 1581 cm^{-1} (COO^- asymmetric stretching backbone in F-G-F-G) may suggest that F or G is in the part of the random coil, fibril, or core β-sheet and plays a key role in inducing protein−protein interaction, forming

https://doi.org/10.1021/acs.langmuir.3c02923
Langmuir 2024, 40, 1728−1746

gold aggregates. If a G-G sequence was involved here, it is likely to be 37Gly-38Gly. Because gold colloids may inhibit the full formation of fibrils, random coils or core β-sheets are more plausible assignments for mode $(iv)_{20}$. Then, most type iv modes were in the latter stage II, and no new mode was observed up to early stage III (see Figure S4a). The most prominent mode in type v was $(v)_{20}$ 1533 cm^{-1}, and this mode was an icon of random coils or core β-sheet. Continuing from type iv modes, we found the observed modes at 1312 and 1581 cm^{-1} implied the involvement of F and G for enhancing aggregation. The mode at 1367 cm^{-1} also suggests β-sheet bending and the involvement of the COO^- symmetric stretching of glutamic acid (Glu or E) or aspartic acid (Asp or D) and CH_2 scissoring, CH_3 symmetric bending, or deformation in A-A. The experimentally covered ϕ value for 20 nm gold reached ~18 $\mu mol/m^2$, which is estimated to be the entrance region of stage III but not further in its stage. Because there was no sign of a new mode growing around $\phi \sim 18$, it is conceivable that type iv modes (i.e., random coil or core β-sheet) are responsible in stage III.

Quite interestingly, the SERS contour map of 80 nm gold was very different from that of 20 nm gold (see panels a−d of Figure 6) and suggested the involvement of different sequences in adsorption as well as aggregation. However, the type i mode at an initial stage ($\phi = 0$) was very similar, and the $(i)_{80}$ 276 cm^{-1} mode was assigned as the vibrational mode of gold clusters ($Au_{n=5,\ 6,\ 15,\ 16,\ 20,\ or\ 58}$). As shown in panels e and f of Figure 6, mode $(i)_{80}$ stayed under a wider region compared to that of mode $(i)_{20}$, which may suggest the more open surface of 80 nm gold allowing more Aβ_{1-40} monomers (or more distance between adjacent Aβ_{1-40} monomers) compared to the case of the 20 nm gold surface. For the region including beyond $\phi = 12$ $\mu mol/m^2$, the SERS signals of the representative modes are shown in panels a and b of Figure S7. In the region around $\phi = 0$, several bands appeared and disappeared within $\phi \sim 0.1$ $\mu mol/m^2$ and were labeled as mode i′. The representative mode $(i)'_{80}$ was observed at 1561 cm^{-1} assigned as Au−COO^- stretching, and another mode i′ with significant intensity was observed at 1095 cm^{-1}, indicating C−N stretching or C−C stretching. While no particular sequence can be identified, these modes indicate triggering of the adsorption process, and they were replaced by modes of type ii. The representative type ii mode [$(ii)_{80}$ 1590 cm^{-1}] belongs to ring C−C stretching of F or possibly Y, showing the involvement of the benzene ring in the induction of adsorption, which is very different from the case observed in 20 nm gold. The mode at 1505 cm^{-1} suggests the NH deformation or C═C asymmetric stretching of H. As another significant type ii mode, that at 1534 cm^{-1} is assigned as the COO^-−Au or COO^- asymmetric stretching backbone, random coils, or β-sheets. Considering the involvement of random coil or β-sheet duing the later stage II or early stage III in 20 nm gold, the involvement of COO^-−Au is more plausible as a role of mode $(ii)_{80}$. At the later stage III ($\phi \sim 2.5$), mode type iii represented by $(iii)_{80}$ 1521 cm^{-1} (NH deformation of 6His, 13His, or 14His, C═C asymmetric stretching) was strongly observed. The modes at 650 cm^{-1} strongly suggest the C−S stretching of methionine (Met or M) at 35Met or the COO^- bending of tyrosine (10Tyr). During stage II, there were many more modes observed for 80 nm gold than for 20 nm gold, and the most prominent was $(iv)_{80}$ 1276 cm^{-1} [CH_2 bending or CH_2 wagging of glutamine (Glu or Q)]. Other significant type iv modes could be 646 cm^{-1} (C−S stretching in 35Met or COO^- bending in 10Tyr) and 1037 cm^{-1} (C−N stretching in 33Gly-34Leu, L-37Gly-38Gly, or G or in-plane ring C−H deformation in 37Gly-38Gly-F or F-G-F-G). Thus, induction of adsorption may continue with a benzene ring-containing sequence such as F or Y, and the formation of protein−protein interactions may be induced by Q, M, or L-G. A remarkable difference from 20 nm gold was also found in the appearance of newly grown modes during stage III, and $(v)_{80}$ 1541 cm^{-1} (COO^- asymmetric stretching backbone, random coils, and core β-sheet). Random coils or core β-sheets must be playing a key role in the assembly of gold aggregates for both 20 and 80 nm gold. However, one dissimilarity was that mode $(v)_{80}$ appeared significantly beyond $\phi \sim 13$ $\mu mol/m^2$ while mode $(v)_{20}$ appeared significantly around $\phi \sim 5$ $\mu mol/m^2$. Although there were several other significant modes, most of them were associated with those in type iv modes observed in stage II.

The major unanswered question is what major interaction makes Aβ_{1-40} bind to the gold colloid surface. Considering that Aβ_{1-40} monomer-coated gold nanoparticles dissolve under aqueous conditions, the hydrophilic segment of the Aβ_{1-40} monomer appears to be facing the aqueous phase. More exactly, a recent study indicated that 28Lys (lysine, Lys, or K) appears to be responsible for an electrostatic interaction with the negative surface of gold nanoparticles[141] and the hydrophobic segment of the peptide must be utilized for adsorption to the gold surface. Thus, peptide networking is considered to take place through hydrophilic segments of peptides, and a high affinity between unfolded amyloidogenic peptides is thought to cause aggregation of peptide-coated gold nanoparticles. This appears to be dependent on the structure of the protein because the unfolded conformation of the peptide repels the peptide-coated nanogold colloids.[153,154]

The ϕ-dependent mode analysis concluded that an intrinsic difference in the formation of gold colloid aggregates between 20 and 80 nm gold originated from the adsorption taking place during early stage I corresponding to $\phi \sim 0.2$ $\mu mol/m^2$. It is conceivable that physical restriction of the available adsorbable surface and the interaction distance between adjacent monomers approaching the surface could favor the 20 nm gold surface being approached by histidine (see the right bottom box of Figure 6e). Differences in these conditions could allow the approach of the 80 nm gold surface by the planelike benzene ring, possibly tyrosine (10Tyr) or phenylalanine (see the right bottom box of Figure 6f). While a random coil or core β-sheet conformation was considered to be the responsible for protein−protein interaction forming aggregates regardless of nanoparticle size, the 80 nm gold generated aggregation at much higher ϕ values, which suggests that the physical property of the gold played a key role in aggregation. This factor can be important for determining the terminal size of gold colloid aggregates, as shown in Figure 2iv. We speculate that the random coil or core β-sheet conformation at the relatively lower ϕ seen in 20 nm gold may lead to further networking between random coils or β-sheets of surrounding preexisting gold aggregates. The 80 nm gold, in contrast, appears to require more monomers to start forming random coil or β-sheet.

CONCLUSIONS

We have established a methodology for investigating the protein−protein interaction involved in the aggregation of the gold nanoparticles possessing a protein corona by using Aβ_{1-40}. By varying the concentration of Aβ_{1-40}, N(Aβ_{1-40}), we were able to define the aggregation process. Thus, this approach reveals the progress of protein−protein interactions or the process of protein interactions. The degree of the SPR peak shift was

https://doi.org/10.1021/acs.langmuir.3c02923
Langmuir 2024, 40, 1728−1746

interpreted as protein aggregation and was calculated as a function of $N(A\beta_{1-40})$ per available gold surface, ϕ. The degree of aggregation was reasonably characterized by the heterogeneous surface coverage ratio, θ, using the Langmuir−Freundlich model, with a significant discrepancy at $0.8 < \theta < 1.0$ implying the involvement of protein−protein interactions. We report a newly found Raman shift peak at 275 ± 5 cm^{-1}, which could be evidence of the presence of gold colloid clusters but not gold colloid aggregates, regardless of the size of the gold colloid. We speculate that the size difference affected the initial adsorption stage because of the difference in the availability of the open gold surface affecting the degree of interaction of $A\beta_{1-40}$ peptides with adjacent monomers. The induction of adsorption for 20 nm gold may be caused by a relatively small contact area (possibly by a part of the −C−N or C═C bond of histidine), while 80 nm gold could be more available to a benzene ring plane (possibly tyrosine or phenylalanine) occupying more contact area with the particle surface. The β-sheet and α-random coil were found to be the key conformations for completing aggregates regardless of the nanosize. The methodology employed in this work can be applied to other amyloidogenic peptides such as α-synuclein or β-2 microglobulin to investigate the aggregation process. This work has great potential for the development and design of sensitive devices for measuring the concentration of amyloidogenic peptides.

■ ASSOCIATED CONTENT

Supporting Information

The Supporting Information is available free of charge at https://pubs.acs.org/doi/10.1021/acs.langmuir.3c02923.

Representative SERS imaging, pattern of SERS peak appearance, contour maps for the higher ϕ values, spectral profile data, appearance of SERS spectral lines as a function of ϕ, and a list of the observed Raman shifts (PDF)

■ AUTHOR INFORMATION

Corresponding Author

Kazushige Yokoyama − *Department of Chemistry, The State University of New York Geneseo College, Geneseo, New York 14454, United States;* orcid.org/0000-0001-5098-5109; Email: yokoyama@geneseo.edu

Authors

Eli Barbour − *Department of Chemistry, The State University of New York Geneseo College, Geneseo, New York 14454, United States;* Present Address: Department of Biomedical Engineering, Carnegie Mellon University, Pittsburgh, PA 15213

Rachel Hirschkind − *Department of Chemistry, The State University of New York Geneseo College, Geneseo, New York 14454, United States*

Bryan Martinez Hernandez − *Department of Chemistry, The State University of New York Geneseo College, Geneseo, New York 14454, United States*

Kaylee Hausrath − *Department of Chemistry, The State University of New York Geneseo College, Geneseo, New York 14454, United States;* Present Address: Jacob School of Medicine, University at Buffalo, Buffalo, NY 14203

Theresa Lam − *Department of Chemistry, The State University of New York Geneseo College, Geneseo, New York 14454, United States;* Present Address: Queens College, City College of New York, Queens, NY 11364

Complete contact information is available at: https://pubs.acs.org/10.1021/acs.langmuir.3c02923

Author Contributions

†E.B., R.H., B.M.H., K.H., and T.L. contributed equally to this work.

Notes

The authors declare no competing financial interest.

■ ACKNOWLEDGMENTS

This work was supported by National Science Foundation Grant 2117780-MRI. T.L. and K.H. are thankful for the SUNY Geneseo Chemistry Department Alumni Summer Research Fellowship (Gerry Rhodes and Kenneth Lipkowitz Fellowship). B.M.H. is thankful for the McNair Scholarship. K.Y. greatly thanks Professor Saburo Matsumoto, Dr. Jonathan Bourne, and Dr. Thomas Gallagher for helpful and stimulating discussion during the preparation of the manuscript. K.Y. is grateful to the Geneseo Foundation for the support during the initial stage of this project and Philip Carubia at the Cornell Center for Material Research of Cornell University. The preliminary data for Raman imaging were tested at the Cornell Center for Materials Research shared Facilities, which are supported through the NSF MRSEC program (DMR-1719875). This study was performed as part of the Cooperative Research Program for the Institute for Protein Research, Osaka University (CR-14-02). K.Y. thanks Professor Yuji Goto for suggesting the idea of this study and the Institute for Protein Research, Osaka University, for International Collaborative Research, 2014.

■ ABBREVIATIONS

TEM, transmission electron microscopy; $A\beta_{1-40}$, amyloid β 1−40; SPR, surface plasmon resonance; SERS, surface-enhanced Raman scattering

■ REFERENCES

(1) Chiti, F.; Dobson, C. M. Protein misfolding, functional amyloid, and human disease. *Annu. Rev. Biochem.* **2006**, *75*, 333−366.

(2) Iadanza, M. G.; Jackson, M. P.; Hewitt, E. W.; Ranson, N. A.; Radford, S. E. A new era for understanding amyloid structures and disease. *Nat. Rev. Mol. Cell Biol.* **2018**, *19*, 755−773.

(3) Chiti, F.; Dobson, C. M. Protein Misfolding, Amyloid Formation, and Human Disease: A Summary of Progress Over the Last Decade. *Annu. Rev. Biochem.* **2017**, *86*, 27−68.

(4) Picken, M. M. The Pathology of Amyloidosis in Classification: A. *Review. Acta Haematol.* **2020**, *143*, 322−334.

(5) Sipe, J. D. Amyloidosis. *Annu. Rev. Biochem.* **1992**, *61*, 947−975.

(6) Hayden, E. Y.; Teplow, D. B. Amyloid β-Protein Oligomers and Alzheimer's Disease. *Alzheimer's Res. Ther.* **2013**, *5*, 60.

(7) Torack, R. M. Adult Dementia: History, Biopsy, Pathology. *Neurosurgery* **1979**, *4*, 434−442.

(8) Ristori, E.; Donnini, S.; Ziche, M. New Insights Into Blood-Brain Barrier Maintenance: The Homeostatic Role of β-Amyloid Precursor Protein in Cerebral Vasculature. *Front. Physiol.* **2020**, *11*, 1056.

(9) Kirschner, D. A.; Inouye, H.; Duffy, L. K.; Sinclair, A.; Lind, M.; Selkoe, D. J. Synthetic peptide homologous to.beta. protein from Alzheimer disease forms amyloid-like fibrils in vitro. *Proc. Natl. Acad.Sci. U S A* **1987**, *84*, 6953−6957.

(10) Lomakin, A.; Chung, D. S.; Benedek, G. B.; Kirschner, D. A.; Teplow, D. B. On the nucleation and growth of amyloid-protein fibrils: detection of nuclei and quantitation of rate constants. *Proc. Natl. Acad. Sci. U. S. A.* **1996**, *93*, 1125−1129.

(11) Walsh, D. M.; Lomakin, A.; Benedek, G. B.; Condron, M. M.; Teplow, D. B. Amyloid -protein fibrillogenesis. *J. Biol. Chem.* **1997**, *272*, 22364−22372.
(12) Lambert, M. P.; Barlow, A. K.; Chromy, B. A.; Edwards, C.; Freed, R.; Liosatos, M.; Morgan, T. E.; Rozovsky, I.; Trommer, B.; Viola, K. L.; Wals, P.; Zhang, C.; Finch, C. E.; Krafft, G. A.; Klein, W. L. Diffusible, nonfibrillar ligands derived from A 1−42 are potent central nervous system neurotoxins. *Proc. Natl. Acad. Sci. U S A* **1998**, *95*, 6448−6453.
(13) Bucciantini, M.; Giannoni, E.; Chiti, F.; Baroni, F.; Formigli, L.; Zurdo, J.; Taddei, N.; Ramponi, G.; Dobson, C. M.; Stefani, M. Inherent toxicity of aggregates implies a common mechanism for protein misfolding diseases. *Nature* **2002**, *416*, 507−511.
(14) Walsh, D. M.; Klyubin, I.; Fadeeva, J. V.; Cullen, W. K.; Anwyl, R.; Wolfe, M. S.; Rowan, M. J.; Selkoe, D. J. Naturally Secreted Oligomers of Amyloid β Protein Potently Inhibit Hippocampal Long-Term Potentiation in Vivo. *Nature* **2002**, *416*, 535−539.
(15) Rocha, S.; Krastev, R.; Thunemann, A. F.; Pereira, M. C.; Mohwald, H.; Brezesinski, G. Adsorption of amyloid beta-peptide at polymer surfaces: a neutron reflectivity study. *ChemPhysChem* **2005**, *6*, 2527−2534.
(16) Attanasio, F.; Convertino, M.; Magno, A.; Caflisch, A.; Corazza, A.; Haridas, H.; Esposito, G.; Cataldo, S.; Pignataro, B.; Milardi, D.; Rizzarelli, E. Carnosine inhibits Aβ42 aggregation by perturbing the H-Bond network in and around the central hydrophobic cluster. *ChemBioChem.* **2013**, *14*, 583−592.
(17) Politi, J.; Spadavecchia, J.; Iodice, M.; de Stefano, L. Oligopeptide-heavy metal interaction monitoring by hybrid gold nanoparticle based assay. *Analyst* **2015**, *140*, 149−155.
(18) Moshe, A.; Landau, M.; Eisenberg, D. Preparation of Crystalline Samples of Amyloid Fibrils and Oligomers. *Methods Mol. Biol.* **2016**, *1345*, 201−210.
(19) Scarff, C. A.; Ashcroft, A. E.; Radford, S. E. Characterization of amyloid oligomers by electrospray ionization-ion mobility spectrometry-mass spectrometry (ESI-IMS-MS). *Methods Mol. Biol.* **2016**, *1345*, 115−132.
(20) Jakob-Roetne, R.; Jacobsen, H. Alzheimer's disease: from pathology to therapeutic approaches. *Angew. Chem., Int. Ed.* **2009**, *48*, 3030−3059.
(21) Zheng, L.; Cedazo-Minguez, A.; Hallbeck, M.; Jerhammar, F.; Marcusson, J.; Terman, A. Intracellular distribution of amyloid beta peptide and its relationship to the lysosomal system. *Transl. Neurodegener.* **2012**, *1*, 19−25.
(22) Pauwels, K.; Williams, T. L.; Morris, K. L.; Jonckheere, W.; Vandersteen, A.; Kelly, G.; Schymkowitz, J.; Rousseau, F.; Pastore, A.; Serpell, L. C.; Broersen, K. Structural Basis for Increased Toxicity of Pathological Aβ42:Aβ40 Ratios in Alzheimer Disease. *J. Biol. Chem.* **2012**, *287*, 5650−5660.
(23) Citron, M.; et al. Mutant Presenilins of Alzheimer's Disease Increase Production of 42-Residue Amyloid β-Protein in Both Transfected Cells and Transgenic Mice. *Nat. Med.* **1997**, *3*, 67−72.
(24) Duff, K.; Eckman, C.; Zehr, C.; Yu, X.; Prada, C. M.; Perez-Tur, J.; Hutton, M.; Buee, L.; Harigaya, Y.; Yager, D.; Morgan, D.; Gordon, M. N.; Holcomb, L.; Refolo, L.; Zenk, B.; Hardy, J.; Younkin, S. Increased Amyloid-B42(43) in Brains of Mice Expressing Mutant Presenilin 1. *Nature* **1996**, *383*, 710−713.
(25) Vadukul, D. M.; Gbajumo, O.; Marshall, K. E.; Serpell, L. C. Amyloidogenicity and Toxicity of the Reverse and Scrambled Variants of Amyloid-β 1−42. *FEBS Lett.* **2017**, *591*, 822−830.
(26) Dahlgren, K. N.; Manelli, A. M.; Stine, W. B.; Baker, L. K.; Krafft, G. A.; LaDu, M. J. Oligomeric and Fibrillar Species of Amyloid-β Peptides Differentially Affect Neuronal Viability. *J. Biol. Chem. Commun.* **2002**, *277*, 32046−32053.
(27) Selkoe, D. J. Translating Cell Biology into Therapeutic Advances in Alzheimer's Disease. *Nature* **1999**, *399*, A23−A31.
(28) Younkin, S. G. Evidence That Abeta 42 Is the Real Culprit in Alzheimer's Disease. *Ann. Neurol.* **1995**, *37*, 287−288.
(29) Kayed, R.; Head, E.; Thompson, J. L.; McIntire, T. M.; Milton, S. C.; Cotman, C. W.; Glabe, C. G. Common structure of soluble amyloid oligomers implies common mechanism of pathogenesis. *Science* **2003**, *300* (5618), 486−489.
(30) Williams, T. L.; Johnson, B. R. G.; Urbanc, B.; Jenkins, A. T. A.; Connell, S. D. A.; Serpell, L. C. Aβ42 Oligomers, but Not Fibrils, Simultaneously Bind to and Cause Damage to Ganglioside-Containing Lipid Membranes. *Biochem. J.* **2011**, *439*, 67−77.
(31) Kirschner, D. A.; Abraham, C.; Selkoe, D. J. X-ray diffraction from intraneuronal paired helical filaments and extraneuronal amyloid fibers in Alzheimer disease indicates cross-beta conformation. Proc. *Natl. Acad. Sci. U.S.A.* **1986**, *83*, 503−507.
(32) Inouye, H.; Fraser, P. E.; Kirschner, D. A. Structure of betacrystallite assemblies formed by Alzheimer beta-amyloid protein analogues: analysis by x-ray diffraction. *Biophys. J.* **1993**, *64*, 502−519.
(33) Paravastu, A. K.; Leapman, R. D.; Yau, W. M.; Tycko, R. Molecular structural basis for polymorphism in Alzheimer's betaamyloid fibrils. *Proc. Natl. Acad. Sci. U.S.A.* **2008**, *105*, 18349−18354.
(34) Xiao, Y.; Ma, B.; McElheny, D.; Parthasarathy, S.; Long, F.; Hoshi, M.; Nussinov, R.; Ishii, Y. Aβ(1−42) Fibril Structure Illuminates Self-Recognition and Replication of Amyloid in Alzheimer's Disease. *Nat. Struct. Mol. Biol.* **2015**, *22*, 499−505.
(35) Colvin, M. T.; Silvers, R.; Ni, Q. Z.; Can, T. V.; Sergeyev, I.; Rosay, M.; Donovan, K. J.; Michael, B.; Wall, J.; Linse, S.; Griffin, R. G. Atomic Resolution Structure of Monomorphic Abeta42 Amyloid Fibrils. *J. Am. Chem. Soc.* **2016**, *138*, 9663−9674.
(36) Luhrs, T.; Ritter, C.; Adrian, M.; Riek-Loher, D.; Bohrmann, B.; Dobeli, H.; Schubert, D.; Riek, R. 3D structure of Alzheimer's amyloid-beta(1−42) fibrils. *Proc. Natl. Acad. Sci. U.S.A.* **2005**, *102*, 17342−17347.
(37) Gremer, L.; Scholzel, D.; Schenk, C.; Reinartz, E.; Labahn, J.; Ravelli, R. B. G.; Tusche, M.; Lopez-Iglesias, C.; Hoyer, W.; Heise, H.; Willbold, D.; Schroder, G. F. Fibril structure of amyloid-beta(1−42) by cryo-electron microscopy. *Science* **2017**, *358*, 116−119.
(38) Schmidt, M.; Rohou, A.; Lasker, K.; Yadav, J. K.; Schiene-Fischer, C.; Fandrich, M.; Grigorieff, N. Peptide dimer structure in an Abeta(1−42) fibril visualized with cryo-EM. *Proc. Natl. Acad. Sci. U.S.A.* **2015**, *112*, 11858−11863.
(39) Yu, L.; Edalji, R.; Harlan, J. E.; Holzman, T. F.; Lopez, A. P.; Labkovsky, B.; Hillen, H.; Barghorn, S.; Ebert, U.; Richardson, P. L.; Miesbauer, L.; Solomon, L.; Bartley, D.; Walter, K.; Johnson, R. W.; Hajduk, P. J.; Olejniczak, E. T. Structural characterization of a soluble amyloid beta-peptide oligomer. *Biochemistry* **2009**, *48*, 1870−1877.
(40) Sarkar, B.; Mithu, V. S.; Chandra, B.; Mandal, A.; Chandrakesan, M.; Bhowmik, D.; Madhu, P. K.; Maiti, S. Significant structural differences between transient amyloid-beta oligomers and less-toxic fibrils in regions known to harbor familial Alzheimer's mutations. *Angew. Chem., Int. Ed.* **2014**, *53*, 6888−6892.
(41) Collins, S. R.; Douglass, A.; Vale, R. D.; Weissman, J. S. Mechanism of prion propagation: Amyloid growth occurs by monomer addition. *PLoS Biol.* **2004**, *2* (10), e321.
(42) Sabaté, R.; Gallardo, M.; Estelrich, J. Temperature dependence of the nucleation constant rate in β amyloid fibrillogenesis. *Int. J. Biol. Macromol.* **2005**, *35* (1−2), 9−13.
(43) Niraula, T. N.; Konno, T.; Li, H.; Yamada, H.; Akasaka, K.; Tachibana, H. Pressure-dissociable reversible assembly of intrinsically denatured lysozyme is a precursor for amyloid fibrils. *Proc. Natl. Acad. Sci. U.S.A.* **2004**, *101* (12), 4089−4093.
(44) Malinchik, S. B.; Inouye, H.; Szumowski, K. E.; Kirschner, D. A. Structural Analysis of Alzheimer's β(1−40) Amyloid: Protofilament Assembly of Tubular Fibrils. *Biophys. J.* **1998**, *74*, 537−545.
(45) Petkova, A. T.; Ishii, Y.; Balbach, J. J.; Antzutkin, O. N.; Leapman, R. D.; Delaglio, F.; Tycko, R. A Structural Model for Alzheimer's -Amyloid Fibrils Based on Experimental Constraints from Solid State NMR. *Proc. Natl. Acad. Sci. U.S.A.* **2002**, *99*, 16742−16747.
(46) Petkova, A. T.; Buntkowsky, G.; Dyda, F.; Leapman, R. D.; Yau, W. M.; Tycko, R. Solid State NMR Reveals a PH-Dependent Antiparallel β-Sheet Registry in Fibrils Formed by a β-Amyloid Peptide. *J. Mol. Biol.* **2004**, *335*, 247−260.
(47) Bitan, G.; Kirkitadze, M. D.; Lomakin, A.; Vollers, S. S.; Benedek, G. B.; Teplow, D. B. Amyloid β-Protein (Aβ) Assembly: Aβ40 and

https://doi.org/10.1021/acs.langmuir.3c02923
Langmuir 2024, 40, 1728−1746

Aβ42 Oligomerize through Distinct Pathways. *Proc. Natl. Acad. Sci. U.S.A.* **2003**, *100*, 330−335.
(48) Moore, G. R.; Pettigrew, G. W. *Cytochrome c: Evolutionary Structural and Physicochemical Aspects*; Springer-Verlag: Berlin, 1990.
(49) Sgourakis, N. G.; Merced-Serrano, M.; Boutsidis, C.; Drineas, P.; Du, Z.; Wang, C.; Garcia, A. E. Atomic-Level Characterization of the Ensemble of the Aβ(1−42) Monomer in Water Using Unbiased Molecular Dynamics Simulations and Spectral Algorithms. *J. Mol. Biol.* **2011**, *405*, 570.
(50) Velez-Vega, C.; Escobedo, F. A. Characterizing the structural behavior of selected Abeta-42 monomers with different solubilities. *J. Phys. Chem. B* **2011**, *115*, 4900−4910.
(51) Olubiyi, O. O.; Strodel, B. Structures of the Amyloid β-Peptides. Aβ1−40 and Aβ1−42 as Influenced by pH and a d-Peptide. *J. Phys. Chem. B* **2012**, *116*, 3280.
(52) Rosenman, D. J.; Connors, C. R.; Chen, W.; Wang, C.; Garcia, A. E. Aβ Monomers Transiently Sample Oligomer and Fibril-Like Configurations: Ensemble Characterization Using a Combined MD/NMR Approach. *J. Mol. Biol.* **2013**, *425*, 3338.
(53) Rosenman, D. J.; Wang, C.; Garcia, A. E. Characterization of Aβ Monomers through the Convergence of Ensemble Properties among Simulations with Multiple Force Fields. *J. Phys. Chem. B* **2016**, *120*, 259.
(54) Itoh, S. G.; Yagi-Utsumi, M.; Kato, K.; Okumura, H. Effects of a Hydrophilic/Hydrophobic Interface on Amyloid-β Peptides Studied by Molecular Dynamics Simulations and NMR Experiments. *J. Phys. Chem. B* **2019**, *123*, 160−169.
(55) O'Brien, E. P.; Okamoto, Y.; Straub, J. E.; Brooks, B. R.; Thirumalai, D. Thermodynamic perspective on the dock-lock growth mechanism of amyloid fibrils. *J. Phys. Chem. B* **2009**, *113*, 14421−14430.
(56) Straub, J. E.; Thirumalai, D. Toward a molecular theory of early and late events in monomer to amyloid fibril formation. *Annu. Rev. Phys. Chem.* **2011**, *62*, 437−463.
(57) Schwierz, N.; Frost, C. V.; Geissler, P. L.; Zacharias, M. Dynamics of Seeded Abeta40-Fibril Growth from Atomistic Molecular Dynamics Simulations: Kinetic Trapping and Reduced Water Mobility in the Locking Step. *J. Am. Chem. Soc.* **2016**, *138*, 527−539.
(58) Sasmal, S.; Schwierz, N.; Head-Gordon, T. Mechanism of Nucleation and Growth of Abeta40 Fibrils from All-Atom and Coarse-Grained Simulations. *J. Phys. Chem. B* **2016**, *120*, 12088−12097.
(59) Bacci, M.; Vymetal, J.; Mihajlovic, M.; Caflisch, A.; Vitalis, A. Amyloid β Fibril Elongation by Monomers Involves Disorder at the Tip. *J. Chem. Theory Comput.* **2017**, *13*, 5117.
(60) Buchete, N. V.; Tycko, R.; Hummer, G. Molecular dynamics simulations of Alzheimer's beta-amyloid protofilaments. *J. Mol. Biol.* **2005**, *353*, 804−821.
(61) Baumketner, A.; Krone, M. G.; Shea, J. E. Role of the familial Dutch mutation E22Q in the folding and aggregation of the 15−28 fragment of the Alzheimer amyloid-beta protein. *Proc. Natl. Acad. Sci. U.S.A.* **2008**, *105*, 6027−6032.
(62) Lemkul, J. A.; Bevan, D. R. Assessing the stability of Alzheimer's amyloid protofibrils using molecular dynamics. *J. Phys. Chem. B* **2010**, *114*, 1652−1660.
(63) Okumura, H.; Itoh, S. G. Structural and Fluctuational Difference Between Two Ends of Aβ Amyloid Fibril: MD Simulations Predict Only One End has Open Conformations. *Sci. Rep.* **2016**, *6*, 38422.
(64) Rodriguez, R. A.; Chen, L. Y.; Plascencia-Villa, G.; Perry, G. Thermodynamics of Amyloid-beta Fibril Elongation: Atomistic Details of the Transition State. *ACS Chem. Neurosci.* **2018**, *9*, 783−789.
(65) Davidson, D. S.; Brown, A. M.; Lemkul, J. A. Insights into Stabilizing Forces in Amyloid Fibrils of Differing Sizes from Polarizable Molecular Dynamics Simulations. *J. Mol. Biol.* **2018**, *430*, 3819−3834.
(66) Ilie, I. M.; Caflisch, A. Simulation Studies of Amyloidogenic Polypeptides and Their Aggregates. *Chem. Rev.* **2019**, *119*, 6956−6993.
(67) Okumura, H.; Itoh, S. G. Amyloid fibril disruption by ultrasonic cavitation: nonequilibrium molecular dynamics simulations. *J. Am. Chem. Soc.* **2014**, *136*, 10549−10552.
(68) Hoang Viet, M.; Derreumaux, P.; Nguyen, P. H. Nonequilibrium all-atom molecular dynamics simulation of the bubble cavitation and application to dissociate amyloid fibrils. *J. Chem. Phys.* **2016**, *145*, 174113.
(69) Hoang Viet, M.; Derreumaux, P.; Li, M. S.; Roland, C.; Sagui, C.; Nguyen, P. H. Picosecond dissociation of amyloid fibrils with infrared laser: A nonequilibrium simulation study. *J. Chem. Phys.* **2015**, *143*, 155101.
(70) Okumura, H.; Itoh, S. G.; Nakamura, K.; Kawasaki, T. Role of Water Molecules and Helix Structure Stabilization in the Laser-Induced Disruption of Amyloid Fibrils Observed by Nonequilibrium Molecular Dynamics Simulations. *J. Phys. Chem. B* **2021**, *125*, 4964−4976.
(71) Nguyen, P. H.; Li, M. S.; Stock, G.; Straub, J. E.; Thirumalai, D. Monomer Adds to Preformed Structured Oligomers of Aβ-Peptides by a Two-Stage Dock-Lock Mechanism. *Proc. Natl. Acad. Sci. U.S.A.* **2007**, *104*, 111−116.
(72) Klimov, D. K.; Thirumalai, D. Dissecting the Assembly of Aβ16−22 Amyloid Peptides into Antiparallel β Sheets. *Structure* **2003**, *11*, 295−307.
(73) Hwang, W.; Zhang, S.; Kamm, R. D.; Karplus, M. Kinetic control of dimer structure formation in amyloid fibrillogenesis. *Proc. Natl. Acad. Sci. U.S.A.* **2004**, *101*, 12916−12921.
(74) Gnanakaran, S.; Nussinov, R.; Garcia, A. E. Atomic-level description of amyloid beta-dimer formation. *J. Am. Chem. Soc.* **2006**, *128*, 2158−2159.
(75) Nguyen, P. H.; Li, M. S.; Derreumaux, P. Effects of all-atom force fields on amyloid oligomerization: replica exchange molecular dynamics simulations of the Abeta(16−22) dimer and trimer. *Phys. Chem. Chem. Phys.* **2011**, *13*, 9778−9788.
(76) Okumura, H.; Itoh, S. G. Molecular dynamics simulations of amyloid-beta(16−22) peptide aggregation at air-water interfaces. *J. Chem. Phys.* **2020**, *152*, 095101.
(77) Ngoc, L. L. N.; Itoh, S. G.; Sompornpisut, P.; Okumura, H. Replica-permutation molecular dynamics simulations of an amyloid-β(16−22) peptide and polyphenols. *Chem. Phys. Lett.* **2020**, *758*, 137913.
(78) Tarus, B.; Straub, J. E.; Thirumalai, D. Probing the initial stage of aggregation of the Abeta(10−35)-protein: assessing the propensity for peptide dimerization. *J. Mol. Biol.* **2005**, *345*, 1141−1156.
(79) Itoh, S. G.; Okamoto, Y. Amyloid-β(29−42) dimer formations studied by a multicanonical-multioverlap molecular dynamics simulation. *J. Phys. Chem. B* **2008**, *112*, 2767−2770.
(80) Lu, Y.; Wei, G.; Derreumaux, P. Effects of G33A and G33I mutations on the structures of monomer and dimer of the amyloidbeta fragment 29−42 by replica exchange molecular dynamics simulations. *J. Phys. Chem. B* **2011**, *115*, 1282−1288.
(81) Itoh, S. G.; Okumura, H. Dimerization process of amyloid-β(29−42) studied by the Hamiltonian replica-permutation molecular dynamics simulations. *J. Phys. Chem. B* **2014**, *118*, 11428−11436.
(82) Itoh, S. G.; Okumura, H. Oligomer Formation of Amyloid-β(29−42) from Its Monomers Using the Hamiltonian Replica-Permutation Molecular Dynamics Simulation. *J. Phys. Chem. B* **2016**, *120*, 6555−6561.
(83) Tarus, B.; Tran, T. T.; Nasica-Labouze, J.; Sterpone, F.; Nguyen, P. H.; Derreumaux, P. Structures of the Alzheimer's Wild-Type Abeta1−40 Dimer from Atomistic Simulations. *J. Phys. Chem. B* **2015**, *119*, 10478−10487.
(84) Man, V. H.; Nguyen, P. H.; Derreumaux, P. Conformational Ensembles of the Wild-Type and S8C Abeta1−42 Dimers. *J. Phys. Chem. B* **2017**, *121*, 2434−2442.
(85) Barz, B.; Liao, Q.; Strodel, B. Pathways of Amyloid-beta Aggregation Depend on Oligomer Shape. *J. Am. Chem. Soc.* **2018**, *140*, 319−327.
(86) Liao, Q.; Owen, M. C.; Bali, S.; Barz, B.; Strodel, B. Aβ under stress: the effects of acidosis, Cu2+-binding, and oxidation on amyloid β-peptide dimers. *Chem. Commun.* **2018**, *54*, 7766−7769.
(87) Fatafta, H.; Khaled, M.; Owen, M. C.; Sayyed-Ahmad, A.; Strodel, B. Amyloid-β peptide dimers undergo a random coil to β-sheet transition in the aqueous phase but not at the neuronal membrane. *Proc. Natl. Acad. Sci. U. S. A.* **2021**, *118*, e2106210118.

https://doi.org/10.1021/acs.langmuir.3c02923
Langmuir 2024, 40, 1728−1746

(88) Hou, L.; Shao, H.; Zhang, Y.; Li, H.; Menon, N. K.; Neuhaus, E. B.; Brewer, J. M.; Byeon, I.-J. L.; Ray, D. G.; Vitek, M. P.; Iwashita, T.; Makula, R. A.; Przybyla, A. B.; Zagorski, M. G. Solution NMR Studies of the Aβ(1−40) and Aβ(1−42) Peptides Establish That the Met35 Oxidation State Affects the Mechanism of Amyloid Formation. *J. Am. Chem. Soc.* **2004**, *126*, 1992−2005.
(89) Ke, P. C.; Zhou, R.; Serpell, L. C.; Riek, R.; Knowles, T. P. J.; Lashuel, H. A.; Gazit, E.; Hamley, I. W.; Davis, T. P.; Fändrich, M.; Otzen, D. E.; Chapman, M. R.; Dobson, C. M.; Eisenberg, D. S.; Mezzenga, R. Half a Century of Amyloids: Past, Present and Future. *Chem. Soc. Rev.* **2020**, *49*, 5473−5509.
(90) Granata, D.; Baftizadeh, F.; Habchi, J.; Galvagnion, C.; De Simone, A.; Camilloni, C.; Laio, A.; Vendruscolo, M. The Inverted Free Energy Landscape of an Intrinsically Disordered Peptide by Simulations and Experiments. *Sci. Rep.* **2015**, *5*, 15449.
(91) Nguyen, P. H.; Ramamoorthy, A.; Sahoo, B. R.; Zheng, J.; Faller, P.; Straub, J. E.; Dominguez, L.; Shea, J.-E.; Dokholyan, N. V.; De Simone, A.; Ma, B.; Nussinov, R.; Najafi, S.; Ngo, S. T.; Loquet, A.; Chiricotto, M.; Ganguly, P.; McCarty, J.; Li, M. S.; Hall, C.; Wang, Y.; Miller, Y.; Melchionna, S.; Habenstein, B.; Timr, S.; Chen, J.; Hnath, B.; Strodel, B.; Kayed, R.; Lesné, S.; Wei, G.; Sterpone, F.; Doig, A. J.; Derreumaux, P. Amyloid Oligomers: A Joint Experimental/Computational Perspective on Alzheimer's Disease, Parkinson's Disease, Type II Diabetes, and Amyotrophic Lateral Sclerosis. *Chem. Rev.* **2021**, *121*, 2545−2647.
(92) Baftizadeh, F.; Biarnes, X.; Pietrucci, F.; Affinito, F.; Laio, A. Multidimensional View of Amyloid Fibril Nucleation in Atomistic Detail. *J. Am. Chem. Soc.* **2012**, *134* (8), 3886−3894.
(93) Baftizadeh, F.; Pietrucci, F.; Biarnes, X.; Laio, A. Nucleation Process of a Fibril Precursor in the C-Terminal Segment of Amyloid-beta. *Phys. Rev. Lett.* **2013**, *110* (16), 168103−168107.
(94) Cabriolu, R.; Kashchiev, D.; Auer, S. Atomistic theory of amyloid fibril nucleation. *J. Chem. Phys.* **2010**, *133* (22), 225101.
(95) Morris, A. M.; Watzky, M. A.; Finke, R. G. Protein aggregation kinetics, mechanism, and curve-fitting: A review of the literature. *Biochimica Et Biophysica Acta-Proteins and Proteomics* **2009**, *1794* (3), 375−397.
(96) Crespo, R.; Rocha, F. A.; Damas, A. M.; Martins, P. M. A Generic Crystallization-like Model That Describes the Kinetics of Amyloid Fibril Formation. *J. Biol. Chem.* **2012**, *287* (35), 30585−30594.
(97) Ferrone, F. A.; Hofrichter, J.; Sunshine, H. R.; Eaton, W. A. Kinetic-Studies on Photolysis-Induced Gelation of Sickle-Cell Hemoglobin Suggest a New Mechanism. *Biophys. J.* **1980**, *32* (1), 361−380.
(98) Xue, W. F.; Homans, S. W.; Radford, S. E. Systematic analysis of nucleation-dependent polymerization reveals new insights into the mechanism of amyloid self-assembly. *Proc. Natl. Acad. Sci. U.S.A.* **2008**, *105* (26), 8926−8931.
(99) Li, M. S.; Kloczkowski, A.; Cieplak, M.; Kouza, M. *Computer simulations of aggregation of proteins and peptides*; Humana Press: Totowa, NJ, 2022.
(100) Roberts, C. J. Non-native protein aggregation kinetics. *Biotechnol. Bioeng.* **2007**, *98* (5), 927−938.
(101) Ferrone, F. A. Analysis of protein aggregation kinetics. *Amyloid, Prions, and Other Protein Aggregates* **1999**, *309*, 256−274.
(102) Ferrone, F. A.; Hofrichter, J.; Eaton, W. A. Kinetics of sickle hemoglobin polymerization. II. A double nucleation mechanism. *J. Mol. Biol.* **1985**, *183* (4), 611−631.
(103) Morris, A. M.; Watzky, M. A.; Agar, J. N.; Finke, R. G. Fitting neurological protein aggregation kinetic data via a 2-step, Minimal/"Ockham's Razor" model: The Finke-Watzky mechanism of nucleation followed by autocatalytic surface growth. *Biochemistry* **2008**, *47* (8), 2413−2427.
(104) Knowles, T. P. J.; Waudby, C. A.; Devlin, G. L.; Cohen, S. I. A.; Aguzzi, A.; Vendruscolo, M.; Terentjev, E. M.; Welland, M. E.; Dobson, C. M. An Analytical Solution to the Kinetics of Breakable Filament Assembly. *Science* **2009**, *326* (5959), 1533−1537.
(105) Tanaka, M.; Collins, S. R.; Toyama, B. H.; Weissman, J. S. The physical basis of how prion conformations determine strain phenotypes. *Nature* **2006**, *442* (7102), 585−589.
(106) Cohen, S. I. A.; Linse, S.; Luheshi, L. M.; Hellstrand, E.; White, D. A.; Rajah, L.; Otzen, D. E.; Vendruscolo, M.; Dobson, C. M.; Knowles, T. P. J. Proliferation of amyloid-β42 aggregates occurs through a secondary nucleation mechanism. *Proc. Natl. Acad. Sci. U.S.A.* **2013**, *110* (24), 9758−9763.
(107) Meisl, G.; Yang, X.; Hellstrand, E.; Frohm, B.; Kirkegaard, J. B.; Cohen, S. I. A.; Dobson, C. M.; Linse, S.; Knowles, T. P. J. Differences in nucleation behavior underlie the contrasting aggregation kinetics of the Aβ40 and Aβ42 peptides. *Proc. Natl. Acad. Sci. U.S.A.* **2014**, *111* (26), 9384−9389.
(108) Leite, J. P.; Gimeno, A.; Taboada, P.; Jiménez-Barbero, J. J.; Gales, L. Dissection of the key steps of amyloid-β peptide 1−40 fibrillogenesis. *Int. J. Biol. Macromol.* **2020**, *164*, 2240−2246.
(109) Majzik, A.; Fülöp, L.; Csapó, E.; Bogár, F.; Martinek, T.; Penke, b. B.; Bíró, G.; Dékány, I. Functionalization of gold nanoparticles with amino acid, -amyloid peptides and fragment. *Colloids Surf., B* **2010**, *81*, 235−241.
(110) Liu, L.; Zhao, F.; Ma, F.; Zhang, L.; Yang, S.; Xia, N. Electrochemical detectionof β-amyloid peptides on electrode covered with N-terminus-specific antibody based on electrocatalytic O2 reduction by Aβ(1−16)-heme-modified gold nanoparticles. *Biosens. Bioelectron.* **2013**, *49*, 231−235.
(111) Elbassal, E. A.; Morris, C.; Kent, T. W.; Lantz, R.; Ojha, B.; Wojcikiewicz, E. P.; Du, D. Gold Nanoparticles as a Probe for Amyloid-β Oligomer and Amyloid Formation. *J. Phys. Chem. C* **2017**, *121*, 20007−20015.
(112) Olmedo, I.; Araya, E.; Sanz, F.; Medina, E.; Arbiol, J.; Toledo, P.; Álvarez-Lueje, A.; Giralt, E.; Kogan, M. J. How changes in the sequence of the peptide CLPFFD-NH2 can modify the conjugation and stability of gold nanoparticles and their affinity for beta-amyloid fibrils. *Bioconjugate Chem.* **2008**, *19*, 1154−1163.
(113) Xu, Y.; Li, Y.; Wei, L.; Liu, H.; Qiu, J.; Xiao, L. Attenuation of the aggregation and neurotoxicity of amyloid peptides with neurotransmitter-functionalized ultra-small-sized gold nanoparticles. *Engineered Science* **2019**, *6*, 53−63.
(114) John, T.; Gladytz, A.; Kubeil, C.; Martin, L. L.; Risselada, H. J.; Abel, B. Impact of nanoparticles on amyloid peptide and protein aggregation: A review with a focus on gold nanoparticles. *Nanoscale* **2018**, *10*, 20894−20913.
(115) Li, J.; Han, Q.; Wang, X.; Yu, N.; Yang, L.; Yang, R.; Wang, C. Reduced aggregation and cytotoxicity of amyloid peptides by graphene oxide/gold nanocomposites prepared by pulsed laser ablation in water. *Small* **2014**, *10* (21), 4386−4394.
(116) Araya, E.; Olmedo, I.; Bastus, N. G.; Guerrero, S. n.; Puntes, V. c. F.; Giralt, E.; Kogan, M. J. Gold nanoparticles and microwave irradiation Inhibit beta-amyloid amyloidogenesis. *Nanoscale Res. Lett.* **2008**, *3*, 435−443.
(117) Hooshmand, N.; Thoutam, A.; Anikovskiy, M.; Labouta, H. I.; El-Sayed, M. Localized surface plasmon resonance as a tool to study protein corona formation on nanoparticles. *J. Phys. Chem. C* **2021**, *125*, 24765−24776.
(118) Huang, W.; Xiao, G.; Zhang, Y.; Min, W. Research progress and application opportunities of nanoparticle-protein corona complexes. *Biomedicine and Pharmacotherapy* **2021**, *139*, 111541−111559.
(119) Latreille, P.-L.; Le Goas, M.; Salimi, S.; Robert, J.; De Crescenzo, G.; Boffito, D. C.; Martinez, V. A.; Hildgen, P.; Banquy, X. Scratching the surface of the protein corona: Challenging measurements and controversies. *ACS Nano* **2022**, *16* (2), 1689−1707.
(120) Neagu, M.; Piperigkou, Z.; Karamanou, K.; Engin, A. B.; Docea, A. O.; Constantin, C.; Negrei, C.; Nikitovic, D.; Tsatsakis, A. Protein bio-corona: critical issue in immune nanotoxicology. *Arch. Toxicol.* **2017**, *91*, 1031−1048.
(121) Sahneh, D. F.; Scoglio, C.; Riviere, J. Dynamics of nanoparticleprotein corona complex formation: analytical results from population balance equations. *PLoS One* **2013**, *8* (5), No. e64690.

https://doi.org/10.1021/acs.langmuir.3c02923
Langmuir 2024, 40, 1728−1746

(122) Boraschi, D.; Italiani, P.; Palomba, R.; Decuzzi, P.; Duschl, A.; Fadeel, B.; Moghimi, S. M. Nanoparticles and innate immunity: New perspectives on host defence. *Semin. Immunol.* **2017**, *34*, 33−51.
(123) Farrera, C.; Fadeel, B. It takes two to tango: understanding the interactions between engineered nanomaterials and the immune system. *Eur. J. Pharm. Biopharm.* **2015**, *95*, 3−12.
(124) Zhdanov, V. P.; Kasemo, B. Monte Carlo simulation of the kinetics of protein adsorption. *Proteins: Struct., Funct., Genet.* **1998**, *30*, 177−182.
(125) Miller, A. E.; Petersen, P. B.; Hollars, C. W.; Saykally, R. J.; Heyda, J.; Jungwirth, P. Behavior of β-Amyloid 1−16 at the air-water interface at varying pH by nonlinear spectroscopy and molecular dynamics simulations. *J. Phys. Chem. A* **2011**, *115*, 5873−5880.
(126) Barrow, C. J.; Yasuda, A.; Kenny, P. T.; Zagorski, M. G. Solution conformations and aggregational properties of synthetic amyloid beta-peptides of Alzheimer's disease. Analysis of circular dichroism spectra. *J. Mol. Biol.* **1992**, *225*, 1075−1093.
(127) Roher, A. E.; Chaney, M. O.; Kuo, Y. M.; Webster, S. D.; Stine, W. B.; Haverkamp, L. J.; Woods, A. S.; Cotter, R. J.; Tuohy, J. M.; Krafft, G. A.; Bonnell, B. S.; Emmerling, M. R. Morphology and toxicity of A -(1−42) dimer derived from neuritic and vascular amyloid deposits of Alzheimer's disease. *J. Biol. Chem.* **1996**, *271*, 20631−20635.
(128) Yokoyama, K. Nanoscale Protein Conjugation. In *Advances in Nanotechnology*; Chen, E. J.; Peng, N., Ed.; Nova Science Publishing: New York, NY, 2010; Vol. *1*, pp. 65−104.
(129) Yokoyama, K. Modeling of reversible protein conjugation on nanoscale surface. In *Computational Nanotechnology: Modeling and Applications with MATLAB*; Musa, S. M., Ed.; CRC Press: Boca Raton, FL, 2011; pp 381−409.
(130) Yokoyama, K. Nano size dependent properties of colloidal surfaces. In *Colloids: Classification, Properties and Applications*; Ray, P. C., Ed.; Nova Publishers, 2012; pp 25−58.
(131) Yokoyama, K. Controlling Reversible Self Assembly Path of Amyloid Beta Peptide over Gold Colloidal nanoparticle's Surface. In *Nanoscale Spectroscopy with Applications*; Musa, S. M., Ed.; CRC Press-Taylor and Francis Group, LLC: Boca Raton, FL, 2013; pp 279−304.
(132) Yokoyama, K.; Briglio, N. M.; Sri Hartati, D.; Tsang, S. M. W.; MacCormac, J. E.; Welchons, D. R. Nanoscale size dependence in the conjugation of amyloid beta and ovalbumin proteins on the surface of gold colloidal particles. *Nanotechnology* **2008**, *19* (10), 375101−375108.
(133) Yokoyama, K.; Welchons, D. R. The conjugation of amyloid beta protein on the gold colloidal nanoparticles' surfaces. *Nanotechnology* **2007**, *18*, 105101−105107.
(134) Eliezer, D. *Protein amyloid aggregation: Methods and Protocols*; Humana Press: Totowa, NJ, 2016.
(135) *Amyloid proteins: methods and protocols*; Humana Press: Totowa, NJ, 2012.
(136) Sigurdsson, E. M.; Calero, M.; Gasset, M. *Amyloid proteins: methods and protocols*; Humana Press: Totowa, NJ, 2012.
(137) Sandal, M. *International Review of Cell and Molecular Biology: Early stage protein misfolding and amyloid aggregation*; Academic Press, 2017.
(138) Uversky, V. N.; Fink, A. L. *Protein misfolding, aggregation, and conformational diseases. Part B, Molecular mechanisms of conformational diseases*; Springer, 2019.
(139) Yokoyama, K.; Gaulin, N. B.; Cho, H.; Briglio, N. M. Temperature Dependence of Conjugation of Amyloid Beta Peptide on the Gold Colloidal Nanoparticles. *J. Phys. Chem. A* **2010**, *114*, 1521−1528.
(140) Azizian, S.; Eris, S. Adsorption isotherms and kinetics. In *Adsorption: Fundamental Processes and Applications*; Ghaedi, M., Ed.; Academic Press: London, 2021.
(141) Yokoyama, K.; Brown, K.; Shevlin, P.; Jenkins, J.; D'Ambrosio, E.; Ralbovsky, N.; Battaglia, J.; Deshmukh, I.; Ichiki, A. Examination of adsorption orientation of amyloidogenic peptides over nano-gold colloidal particles' surfaces. *International Journal of Molecular Science* **2019**, *20* (21), 5354−5380.
(142) Azizian, S.; Eris, S.; Wilson, L. D. Re-evaluation of the century-old Langmuir isotherm for modeling adsorption phenomena in solution. *Chem. Phys.* **2018**, *513*, 99−104.
(143) Yokoyama, K.; Cho, H.; Cullen, S. P.; Kowalik, M.; Briglio, N. M.; Hoops, H. J.; Zhao, Z.; Carpenter, M. A. Microscopic investigation of reversible nanoscale surface size dependent protein conjugation. *International Journal of Molecular Science* **2009**, *10*, 2348−2366.
(144) Gao, P.; Weaver, M. J. Metal-Adsorbate Vibrational Frequencies as a Probe of Surface Bonding: Halides and Pseudohalides at Gold Electrodes. *J. Phys. Chem.* **1986**, *90*, 4057−4063.
(145) Vishwanathan, K.; Springborg, M. A highest stable cluster Au58 (C1) re-optimized via a density-functional tight-binding (DFTB) approach. *RSC Adv.* **2018**, *8*, 11357−11366.
(146) Vishwanathan, K. Symmetry of Gold Neutral Clusters Au3−20 and Normal Modes of Vibrations by using the Numerical Finite Difference Method with Density-Functional Tight-Binding (DFTB) Approach. *Arch. Chem. Res.* **2017**, *2* (14), 1−17.
(147) Talaga, D.; Cooney, G. S.; Ury-Thiery, V.; Fichou, Y.; Huang, Y.; Lecomte, S.; Bonhommeau, S. Total Internal Reflection Tip-Enhanced Raman Spectroscopy of Tau Fibrils. *J. Phys. Chem. B* **2022**, *126* (27), 5024−5032.
(148) Zhang, Y.; Wang, L.-M.; Tan, E.-Z.; Yang, S.-H.; Li, L.-D.; Guo, L. Uniform arrays of gold nanoparticles with different surface roughness for surface enhanced Raman scattering. *Chin. Chem. Lett.* **2015**, *26*, 1426−1430.
(149) Tinguely, J.-C.; Sow, I.; Leiner, C. Gold Nanoparticles for Plasmonic Biosensing: The Role of Metal Crystallinity and Nano-scaleRoughness. *Bio Nano Science* **2011**, *1*, 128−135.
(150) Trügler, A.; Tinguely, J.-C.; Krenn, J. R.; Hohenau, A.; Hohenester, U. Influence of surface roughness on the optical properties of plasmonic nanoparticles. *Phys. Rev. B* **2011**, *83*, 81412.
(151) Ferraro, J. R. *Low-Frequency Vibrations of Inorganic and Coordination Compounds*; Plenum Press, 1971.
(152) Itoh, S. G.; Yagi-Utsumi, M.; Kato, K.; Okumura, H. Key Residue for Aggregation of Amyloid-β Peptides. *ACS Chem. Neurosci.* **2022**, *13*, 3139−3151.
(153) Yokoyama, K.; Catalfamo, C. D.; Yuan, M. Reversible peptide oligomerization over nanosclae gold surfaces. *AIMS Biophys.* **2015**, *2* (4), 649.
(154) Yokoyama, K.; Chen, H. L.; Islam, A.; Deshmukh, I.; Shevlin, P.; Brown, K.; Ichiki, A. Dynamical Investigation of Adsorption Orientation of Amyloid Beta Peptide 1−40 at Nano-Scale Gold Surface. *BAOJ Chemistry* **2019**, *5* (1), 1−20.
(155) Szekeres, G. P.; Kneipp, J. SERS probing of proteins in gold nanoparticle agglomerates. *Front. Chem.* **2019**, *7*, 1−10.
(156) Lin, V. J. C.; Koenig, J. L. Raman studies of bovine serum albumin. *Biopolymers* **1976**, *15*, 203−218.
(157) Fazio, B.; D'Andrea, C.; Foti, A.; Messina, E.; Irrera, A.; Donato, M.; Villari, V.; Micali, N.; Maragò, O. M.; Gucciardi, P. G. SERS detection of Biomolecules at Physiological pH via aggregation of Gold Nanorods mediated by Optical Forces and Plasmonic Heating. *Sci. Rep.* **2016**, *6*, 26952.
(158) Hornemann, A.; Drescher, D.; Flemig, S.; Kneipp, J. Intracellular SERS hybrid probes using BSA-reporter conjugates. *Anal. Bioanal. Chem.* **2013**, *405*, 6209−6222.
(159) Rygula, A.; Majzner, K.; Marzec, K. M.; Kaczor, A.; Pilarczyk, M.; Baranska, M. Raman spectroscopy of proteins: a review. *J. Raman Spectrosc.* **2013**, *44* (8), 1061−1076.
(160) Stewart, S.; Fredericks, P. M. Surface-enhanced Raman spectroscopy of peptides and proteins adsorbed on an electrochemically prepared silver surface. *Spectrochimica Acta Part A* **1999**, *55*, 1615−1640.
(161) Peticolas, W. L. Raman spectroscopy of DNA and proteins. *Methods Enzymol.* **1995**, *246*, 389−416.
(162) Grys, D.-B.; de Nijs, B.; Salmon, A. R.; Huang, J.; Wang, W.; Chen, W.-H.; Scherman, O. A.; Baumberg, J. J. Citrate Coordination and Bridging of Gold Nanoparticles: The Role of Gold Adatoms in AuNP Aging. *ACS Nano* **2020**, *14*, 8689−8696.

https://doi.org/10.1021/acs.langmuir.3c02923
Langmuir 2024, 40, 1728−1746

(163) Dong, J.; Atwood, C. S.; Anderson, V. E.; Siedlak, S. L.; Smith, M. A.; Perry, G.; Carey, P. R. Metal binding and oxidation of Amyloid-beta within isolated senile plaque cores: Raman microscopic evidence. *Biochemistry* **2003**, *42*, 2768−2773.
(164) Carey, P. R. *Biochemical Applications of Raman and Resonance Raman Spectroscopies*; Academic Press: New York, 1982.
(165) Harada, I.; Takeuchi, H. Raman and ultraviolet resonance Raman spectra of proteins and related compounds. In *Spectroscopy of Biological Systems: Advances in Infrared and Raman Spectroscopy*; Clark, R. J. H., Hester, R. E., Eds.; Wiley: Chichester, U.K., 1986; Vol. *13*, pp 113−175.
(166) Overman, S. A.; Thomas, G. J., Jr. Raman markers of nonaromatic side chains in an R-helix assembly: Ala, Asp, GGly, Ile, Leu, Lys, Ser, and Val residues of phage fd subunits,lu. *Biochemistry* **1999**, *38*, 4018−4027.
(167) Yu, X.; Hayden, E. Y.; Xia, M.; Liang, O.; Cheah, L.; Teplow, D. B.; Xie, Y.-H. Surface enhanced Raman spectroscopy distinguishes amyloid B-protein isoforms and conformational states. *Protein Sci.* **2018**, *27*, 1427−1438.
(168) Palombo, F.; Tamagnini, F.; Jeynes, J. C. G.; Mattana, S.; Swift, I.; Nallala, J.; Hancock, J.; Brown, J. T.; Randall, A. D.; Stone, N. Detection of Aβ plaque-associated astrogliosis in Alzheimer's disease brain by spectroscopic imaging and immunohistochemistry. *Analyst* **2018**, *143* (4), 850−857.
(169) Madzharova, F.; Heiner, Z.; Kneipp, J. Surface enhanced hyper Raman scattering (SEHRS) and its applications. *Chem. Soc. Rev.* **2017**, *46*, 3980−3999.
(170) Walther, M.; Plochocka, P.; Fischer, B.; Helm, H.; Uhd Jepsen, P. Collective vibrational modes in biological molecules investigated by terahertz time-domain spectroscopy. *Biopolymers (Biospectroscopy)* **2002**, *67*, 310−313.
(171) Guo, T.; Ding, F.; Li, D.; Zhang, W.; Cao, L.; Liu, Z. Full-Scale Label-Free Surface-Enhanced Raman Scattering Analysis of Mouse Brain Using a Black Phosphorus-Based Two-Dimensional Nanoprobe. *Applied Sciences* **2019**, *9*, 398−408.
(172) Stiebing, C.; Jahn, I. J.; Schmitt, M.; Keijzer, N.; Kleemann, R.; Kiliaan, A. J.; Drexler, W.; Leitgeb, R. A.; Popp, J. r. Biochemical Characterization of Mouse Retina of an Alzheimer's Disease Model by Raman Spectroscopy. *ACS Chem. Neurosci.* **2020**, *11*, 3301−3308.

https://doi.org/10.1021/acs.langmuir.3c02923
Langmuir 2024, 40, 1728−1746